Research Square

Preprints are preliminary reports that have not undergone peer review.
They should not be considered conclusive, used to inform clinical practice,
or referenced by the media as validated information.

Design and Evaluation of Electrical Motors for Flywheel Energy Storage Systems: A Multi-Criteria Decision Framework for Optimal Selection

Hossein Azizi Moghaddam
Niroo Research Institute
Reza Mirzahosseini
mirzahosseini@jsu.ac.ir
Jundi-Shapur University of Technology

Article

Keywords: Electrical machines, Finite element analysis (FEA), Flywheel energy storage systems (FESSs), TOPSIS multi-criteria decision-making (MCDM) method

Posted Date: November 2nd, 2026

DOI: https://doi.org/10.21203/rs.3.rs-11026999/v1

License: This work is licensed under a Creative Commons Attribution 4.0 International License.
Read Full License

Additional Declarations: No competing interests reported.

DESIGN AND EVALUATION OF ELECTRICAL MOTORS FOR FLYWHEEL ENERGY STORAGE SYSTEMS: A MULTI-CRITERIA DECISION FRAMEWORK FOR OPTIMAL SELECTION

Hossein Azizi Moghaddam[1], Reza Mirzahosseini[2*]

[1]Department of Electrical Machines, Niroo Research Institute, Tehran, Iran
[2]Department of Electrical and Computer Engineering, Jundi-Shapur University of Technology, Dezful, Iran
*Corresponding author: mirzahosseini@jsu.ac.ir

Flywheel energy storage systems (FESSs) are considered one of the most promising options in the field of energy storage because of their high reliability, long lifetime, low maintenance requirements, and fast dynamic response to power fluctuations. The electrical machine, as the heart of FESS, plays a key role in determining its technical and economic characteristics. For this reason, the selection of a suitable structure has a direct influence on the performance, dimensions, cost, and lifetime of the FESS. Therefore, the main objective of this paper is to select the optimal structure of the electrical machine for use in FESS considering the mechanical, magnetic and thermal aspects. Subsequently, a comprehensive design algorithm is presented for various system components containing the electrical machine, bearings, cooling system, and rotating mass. Furthermore, a dedicated algorithm is developed to design the electrical machine according to the FESS application. Based on these two algorithms, thirteen different topologies of electrical machines suitable for FESS applications are designed. The Finite element analysis (FEA) is performed to extract the electromagnetic and thermal characteristics of these topologies. In this paper, two major FESS applications, namely frequency regulation in power systems and electric vehicle applications, are considered. Then, by defining a set of key criteria and applying application-specific weightings, the TOPSIS multi-criteria decision-making (MCDM) method is employed to prioritize the machine structures. The results indicate that the choice of machine topology is strongly dependent on the FESS application and no single topology can be definitively introduced as the best option.

***Keywords*: Electrical machines, Finite element analysis (FEA), Flywheel energy storage systems (FESSs), TOPSIS multi-criteria decision-making (MCDM) method.**

1. Introduction

The increasing demand for energy and the necessity to improve power system reliability have led to the adoption of various power generation methods. In order to maintain the stability of the power grid, the balance between the generated power and the power demanded by the grid is of particular importance. Furthermore, increasing the penetration rate of renewable resources, maintaining grid stability, and generating electricity with acceptable quality will face numerous challenges.

Among the effective solutions for these problems is the use of energy storage systems (ESSs). The application of ESS in combination with other energy production sources, especially renewable sources, has grown significantly in recent years. Various types of energy storage technologies have been proposed, each with its own advantages and disadvantages. In general, no energy storage technology is ideal, and considering the technical and economic characteristics of each, their use is justified for a specific application area. Nowadays, to simultaneously leverage the advantages of various types of ESSs, the combined utilization of various energy storage technologies has become prevalent [1].

Although large-scale energy storage deployment is currently dominated by pumped hydro storage and lithium-ion batteries, flywheel energy storage systems (FESSs) offer unique advantages in terms of fast response, high ramp rate, and long cycle life. As a result, FESS is best utilized as a complementary technology within hybrid ESSs, where it supports high charge and discharge cycle tolerance, fast dynamic response, long life, and low maintenance cost [2]–[4].

One of the key components of a FESS is its electrical machine unit. The FESS energy density and power density, efficiency, cost, lifetime, and reliability are affected by the choice of machine type. Therefore, selecting the appropriate electrical machine type that is used in a FESS for a specific application is an important starting point in optimizing the FESS. So far, extensive research has been conducted in the field of design, selection of structure, performance improvement, and manufacturing of electrical machines used in FESSs. In [5], the design of a FESS consisting of a motor/generator (either a homopolar induction machine (IM)

or a brushless permanent magnet (PM) motor), bearings, a cylindrical flywheel, and high-frequency drives is presented. In this reference, composite materials with low density and high tensile strength are recognized as the best option, as they enable more energy storage per unit mass compared to metals. This reference provides a comparison between different topologies of electrical machines, which helps in making the optimal choice for applications requiring high stability and fast dynamic response.

In [6], the structure of the FESS — including high-speed rotors (up to 60000 rpm), PM motor/generators, magnetic bearings, and vacuum chambers — is reviewed, and its advantages over other technologies such as lithium-ion batteries and supercapacitors are presented. Challenges such as high self-discharge rate and high initial cost — ranging from 300-1000 $/kW of power and 3000-8000 $/kWh of energy — have also been examined, and solutions to reduce them have been proposed. In [7], a machine with a rated power of 3 kW and operating at 9000 rpm has been designed for a FESS used in home applications and connected to small solar systems. For this purpose, three different machine topologies are considered: iron-core PM machine, synchronous reluctance machine (SynRM), and dual-rotor coreless PM machine. The results of finite element analysis (FEA) show that the coreless PM machine with two rotors provides the best performance for domestic applications. It achieves an efficiency of 95.3%, very low no-load losses (0.75 W), a power factor of 0.99 and radial force of only 0.32 N. Due to the absence of an iron core, this machine exhibits lower energy losses during self-discharge and stores approximately 4574 kWh of net energy annually, which is about 255 kWh more than machine with iron core. The authors of [8]–[10] have provided a comprehensive review of FESSs with the aim of using them in high-speed and fast-response applications such as industrial UPS, microgrids, renewable energy sources, and electric vehicles. In these references, various types of electrical machines including interior permanent magnet synchronous machines (IPMSMs), reluctance machines (RM), surface-mounted permanent magnet synchronous machines (SMPMSMs), IMs, permanent magnet-assisted synchronous reluctance (PMASRMs), switched reluctance machines (SRMs), brushless DC motors (BLDCs), SynRMs, homopolar machines (HMs), and bearingless machines are compared for flywheel applications. The comparison focuses on efficiency, torque density, power factor, cost, and high-speed charge/discharge capability. IMs are widely used in power plants and grid stabilization systems due to their simplicity and low cost. RMs, known for their higher efficiency and high current-carrying capacity, are suitable for UPS systems and short-term peak power applications. The FEA results indicate that the IPMSM has an average torque approximately 3.07% higher than that of the SMPMSM and 31.06% higher than that of the SynRM, while the efficiency of both PMSM types (IPMSM and SMPMSM) is approximately 97%. The PMASRM with a neodymium magnet (N30UH) has 30% more torque, 4.7% higher efficiency, and a 37.4% higher power factor than the SynRM, while costing less than the IPMSM. These papers also compare the performance of the motors at high speeds (up to 60000 rpm) and show that the IPMSM and the PMASRM have equivalent performance at output power above 30 kW. From an economic perspective, the PMASRM is the most cost-effective option, whereas IPMSM is the most expensive (with neodymium priced at 126.2 $/kg). In [11], a high-power density PMSM for a FESS is designed. The design includes an axial flux permanent magnet (AFPM) machine with two rotors and a stator. The designed machine is capable of delivering 100 kW of output power within the speed range of 10000 to 20000 rpm. The machine has a power density of about 2.4 kW/kg and an efficiency of up to 95.5%. The use of an integrated hollow rotor and composite materials in the construction has reduced aerodynamic losses and increased power density. The design is proposed for applications requiring fast response, compact size, and high power, such as industrial UPS, transportation, and space systems. In [12], four motor/generator topologies for a FESS with a rated power of 5 kW and an operational speed range of 10000 to 30000 rpm are compared, focusing on long-term energy storage applications. In this study, SRMs, SynRMs, and PMSMs with both internal and external rotor configurations are analyzed using FEA. The results show that the overall losses in SRM are approximately the same at low and high speeds. Also, SynRM machines provide a trade-off between efficiency, copper volume, and manufacturing complexity compared to other options. The results of the study indicate that the PMSM design with an internal rotor, Halbach-array PMs, and coreless structure is the most suitable option for long-term ESSs, provided that the thermal and

mechanical challenges associated with high speeds are addressed. In [13], the structure, performance and design of an AFPM machine for FESS are investigated. Two types of AFPM machines — one with a stator core and the other coreless — are considered and analyzed using the FEA. The results demonstrate that iron-core design is limited by magnetic losses at high frequencies, whereas the coreless configuration can achieve power densities of up to 6 kW/kg and efficiencies exceeding 90% at speeds ranging from 25000 to 50000 rpm. The machine presented in this paper is specifically designed for grid integration applications such as frequency regulation, voltage control, and peak load reduction.

In [14], two types of FESSs were investigated: low-speed (operating below 6000 rpm) and high-speed (up to 100000 rpm) systems. It was shown that high-speed systems with PMSMs, magnetic bearings, and vacuum chambers can achieve a power density of about 12 kW/kg and an efficiency of approximately 95.2%, whereas low-speed systems are cheaper but significantly bulkier. In [15], the performance and loss characteristics of a 100 kW squirrel cage IM-based FESS operating within a speed range of 10000 to 20000 rpm were investigated in the MATLAB/Simulink environment. The results indicate that the standby losses over a period of 20 minutes are less than 215 Wh (equivalent to 3.4% of the stored energy of 5 kWh), with total power dissipation being approximately 5.9%. The paper also compares the advantages and disadvantages of different machines, including IM, PMSM, and SRM. For instance, the efficiency of IM is reported to be about 93.4%, whereas that of PMSM is approximately 95.5%. Although IM has no idling losses and features a robust mechanical structure, its design for high speeds poses challenges. In contrast, PMSM has higher efficiency but is prone to demagnetization. This review indicates that IM is a suitable option for high-power, low-cost, and controllable applications in FESS. In [16], PMSMs have been introduced as the preferred choice for use in FESSs operating at high and variable speeds (up to 100000 rpm) owing to their high power density, high efficiency (up to 98%), and no need for excitation current.

Based on the reviewed literature, different structures of electrical machines can be used in a FESS due to the wide range of its applications. Selecting the optimal machine structure is a challenging task that can cause confusion for the designers. Moreover, some dimensional constraints limit the allowable diameter and length of the machine. In addition, the material of the different components of the machine has a significant impact on its performance characteristics such as losses, efficiency, vibrations and noise. The choice of the machine cooling system significantly influences the temperature of its various components as well as its power density. Additionally, the type of bearings used for the FESS affects the overall losses and efficiency of the system. Although comprehensive multiphysics optimization algorithms for electrical machine design are known to exist in industrial practice, their detailed formulations and results are generally not available in the open literature due to commercial confidentiality. To the best of the authors' knowledge, no comprehensive and openly published design framework has been reported that simultaneously addresses the mechanical, thermal, magnetic, and electrical constraints of electrical machines specifically tailored for FESS applications. Furthermore, no algorithm has yet been proposed for selecting the optimal structure of electrical machines appropriate for each specific application of the FESS. Therefore, the main objective and novelty of the present work are to develop a systematic multi-physics framework for the design and selection of electrical machines for FESS. The novelty of the work lies in (i) the inclusion of mechanical, thermal, magnetic, and electrical constraints in a single design process, (ii) the use of TOPSIS-based multi-criteria decision making to compare different electrical machine topologies under similar operating conditions, and (iii) the demonstration of application-dependent optimal machine selection. For this purpose, section 2 describes the construction of FESS, section 3 introduces the multi-physics design framework, section 4 presents the machine topologies and design assumptions. In addition, section 5 presents simulation results, section 6 provides the TOPSIS analysis, and the limitations and conclusions of the work are presented in section 7. An overview of the paper structure and the contribution of each section has been summarized in Fig. 1.

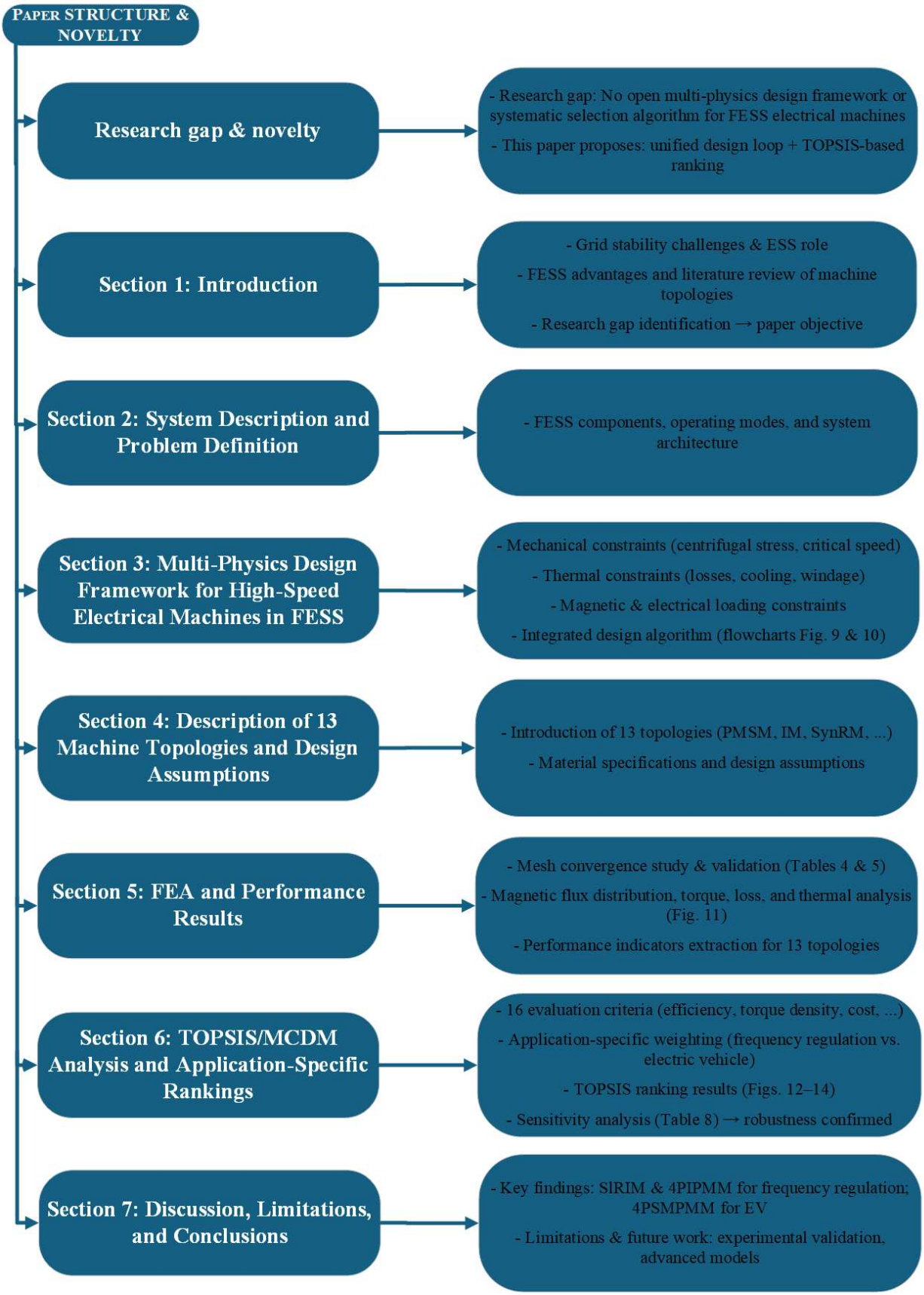


Fig. 1. Structure roadmap of the paper

2. System Description and Problem Definition

Understanding the system-level construction is necessary for the multi-physics design framework presented in section 3. Therfore, in this section, the overall structure of the FESS studied in this paper is described. The general structure of a FESS is depicted in Fig. 2. As shown, the FESS consists of five main components, which are:

- High-power electrical machine
- Flywheel mass
- Active or passive magnetic bearings
- Advanced cooling systems
- Flywheel-side power electronic converter
- A grid-side power electronic converter and a transformer.

The FESS operates in three modes: charging, discharging, and standby. The flywheel-side converter (electrical machine drive system) is controlled so that in charging mode, electrical energy is absorbed from the DC bus and stored as kinetic energy in the rotating disk. During discharge, the drive system operates the electrical machine as a generator so that the kinetic energy of the rotating disk is converted into electrical energy and injected into the DC bus. In this situation, the grid-side converter transfers the energy injected into the DC bus to the AC network. In standby mode, the control system stabilizes the speed of the rotating disk within the permissible range. This is achieved by absorbing a small amount of power from the grid (self-discharge), which imposes limitations on long-term energy storage in the flywheel system [17], [18].

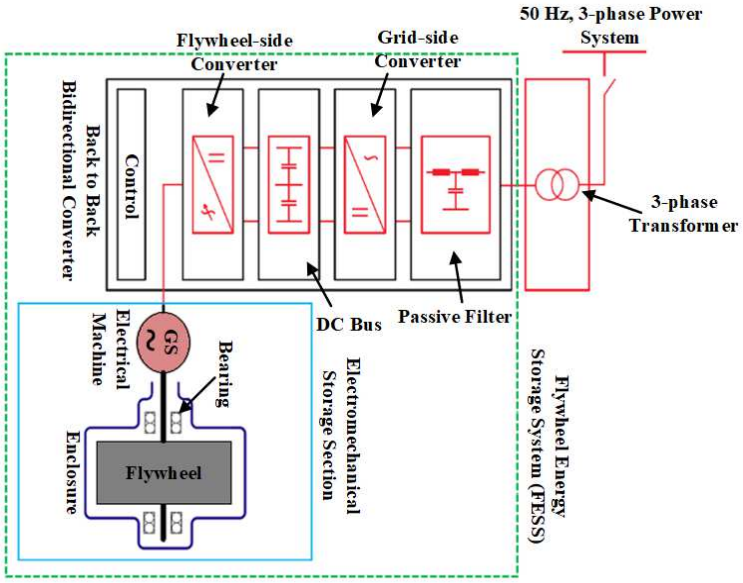


Fig. 2. Schematic structure of the FESS

Fig. 3 illustrates the overall structure of the FESS investigated in this study. In this paper, a cylindrical flywheel energy storage structure is utilized, where the electrical machine and the rotating mass are coupled. The flywheel system modeled in this study uses a vertical shaft configuration, which is widely used in industry. The vertical axis reduces radial loads on bearings, directs centrifugal forces downward improving rotor stability and dynamic behavior, allows more compact floor-space installation, and facilitates the design of containment structures for safety, which are important considerations in designing high-speed flywheel energy storage systems. The suspension system consists of a hybrid magnetic bearing configuration, comprising an active magnetic bearing for damping radial forces and a passive magnetic bearing to support the weight of the rotor assembly and flywheel disk along the axial direction. To ensure safe operation and prevent the disintegration of rotating components in the event of a magnetic

bearing malfunction, two mechanical bearings—supporting both radial and axial loads—are employed as a backup suspension system. The cooling system is mounted on the motor housing [19], [20].

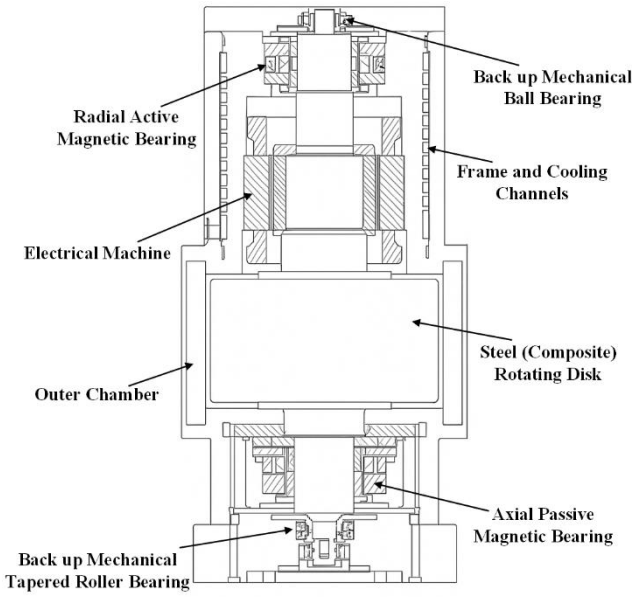


Fig. 3. Overall structure of the FESS [21]

Depending on the technology used, two types of FESSs have been developed: low-speed and high-speed. In low-speed flywheels, the rotating disk is typically made of steel. In such flywheels, the energy-to-power ratio, which corresponds to the discharge time, is relatively low—typically in the range of a few seconds to several minutes. This type of FESS has low cost and features a simple manufacturing process; however, its energy efficiency is relatively low. High weight and large volume are other disadvantages of low-speed FESS. It should be noted that low-speed FESSs differ fundamentally from high-speed designs in terms of mechanical stress and safety requirements. In low-speed FESS, the rotor operates at relatively low rotational speeds, resulting in significantly reduced mechanical stresses and a negligible likelihood of rotor burst. Consequently, the casing system in low-speed designs is not required to serve as a burst containment structure, but primarily provides mechanical support and environmental protection. While this inherent safety advantage is obtained at the cost of significantly greater rotor mass to store a given amount of energy, the higher rotor inertia results in greater bearing loads and thus greater bearing losses, especially for systems using mechanical bearings. Therefore, low-speed FESSs have lower power density and higher parasitic losses than high-speed flywheel systems and are not particularly appealing for applications requiring compactness and high efficiency. In high-speed FESSs, the energy-to-power ratio is in the range of several minutes to a few hours. The design of this type of storage is based on energy capacity. In these systems, the speed of flywheel can be increased by employing high-speed electrical machine technology. Composite rotors were the solution of choice for high-speed FESSs because of their high specific strength, as discussed in the early academic literature. It was largely true before the early 2000s, when the combination of progress in materials, manufacturing processes, and safety-oriented design allowed high-speed steel flywheel rotors to become equally common in commercial applications. Industrial implementations from companies such as Torus Power, Vycon, Amber Kinetics, Temporal Power, and Zooz Power have demonstrated that steel-based flywheel designs are now used at high rotational speeds. In addition, these steel-based designs have significant advantages in terms of thermal conductivity, known failure modes, and reduced safety-related containment requirements. As a result, modern FESSs use a mixture of rotor technologies, including steel, composite, and hybrid steel–composite configurations, based on application needs and safety concerns [22].

In light of these considerations, the design and selection methodology proposed in the present paper is intentionally formulated to be independent of the rotor material choice. The presented multi-physics framework, which simultaneously considers mechanical,

thermal, magnetic, and electrical constraints, is applicable to composite, steel, and hybrid rotor configurations.

One of the individual features of a FESS is the ability to select from a wide range of configurations for each of its subsystems. The design trade-off spectrum in FESS is depicted in Fig. 4, showing the compromise between cost and performance: low-speed designs offer lower cost but larger volume, whereas high-speed designs provide higher compactness at greater cost. The system construction described in this section provides the basis for the design framework presented in section 3. The mechanical, thermal, and electrical limitations presented here are systematically addressed in the multi-physics design algorithm that follows.

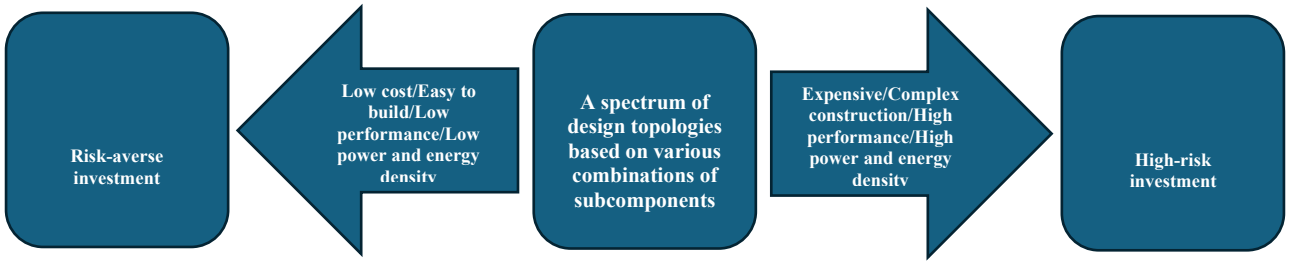


Fig. 4. Design trade-off spectrum in FESS

3. Multi-Physics Design Framework for High-Speed Electrical Machines in FESS

The design of electrical machines for FESS is subject to a number of interrelated mechanical, thermal, magnetic, and electrical constraints. This section describes a multi-physics framework that addresses these constraints. The framework starts with mechanical design, followed by thermal limitations, and finally the electrical and magnetic loading constraints that determine the performance limits of the machine. Understanding these constraints is crucial to the design algorithm outlined in section 3.4.

In a FESS, key performance metrics—such as efficiency, power and energy capacity, and power density—along with the overall cost, are strongly influenced by the choice of electrical machine type, the accuracy of its design, and the quality of manufacturing. Compared to conventional low- and medium-speed electrical machines, high-speed electrical machines offer advantages such as higher power density, smaller size, and reduced weight. More importantly, high-speed electrical machines can be directly coupled to high-speed loads, eliminating the need for conventional gearboxes, which enhances overall efficiency and reliability while minimizing vibration, noise, and cost. With the development of power electronic converters, the requirement for high-frequency sources to enable high-speed operation is no longer a significant constraint. Recent advances in high-speed bearing technologies, characterized by reduced losses, increased rigidity, and extended service life, have enabled the advancement of high-speed electrical machines.

Despite their advantages, high-speed electrical machines face various challenges and limitations in design and manufacturing. These challenges include a wide range of considerations, such as mechanical, electromagnetic, and thermal aspects. Given the complexity and critical importance of these factors in the design process, each of the challenges and limitations will be examined in detail in the following sections to clarify their impact on the structural choices and operational behavior of high-speed machines.

3.1. Mechanical Design constraints and losses

The design of high-speed electrical machines involves following mechanical challenges and constraints that directly affect the machine's performance characteristics and operational lifetime:

Rotor centrifugal stresses and tangential speed: At high rotational speeds, the centrifugal forces exerted on the rotor can lead to rotor deformation and catastrophic failure if they exceed the material's maximum yield strength. According to the nomenclature used in Fig. 5, to ensure the safe operation of an electrical motor with a solid rotor, the maximum allowable outer diameter D_r is calculated as follows [23]:

$$D_r \le \sqrt{\frac{8\sigma_{\max}}{\rho\pi^2 n^2 \left(3+v_p\right)}} \tag{1}$$

Where σ_{max}, ρ, n, and v_p are the maximum yield strength, the mass density, rotor speed, and Poisson's ratio of the rotor material, respectively.

For electrical machines with laminated rotors, the maximum allowable rotor diameter is determined as follows [23]:

$$D_r \le \sqrt{\frac{4\sigma_{\max}}{\rho\pi^2 n^2 \left(3+v_p\right)} - \frac{1-v_p}{3+v_p} d_r^2} \tag{2}$$

Where d_r is the shaft diameter. It should be noted that (2) is derived under the assumption of a laminated rotor with a central shaft hole, corresponding to the classical centrifugal stress analysis of a hollow rotating disk. Although this configuration is widely adopted in laminated rotors, it is not universal. Laminated rotors without a central hole—such as those employed in certain induction motor (IM) designs—also exist. In such cases, the assumptions underlying (2) are no longer satisfied, and the maximum allowable rotor diameter should instead be evaluated using the solid-rotor formulation given in (1). This distinction between solid and hollow rotating disks follows classical rotating disk stress theory [24].

For a rotor core material with specified yield strength, Poisson's ratio, and material density, the maximum allowable tangential speed v_c can be calculated as follows [25], [26]:

$$v_c = \pi D_r n \le \sqrt{\frac{4\sigma_{\max}}{\rho\left[(1-v_p)(\frac{d_r}{D_r})^2 + \left(3+v_p\right)\right]}} \tag{3}$$

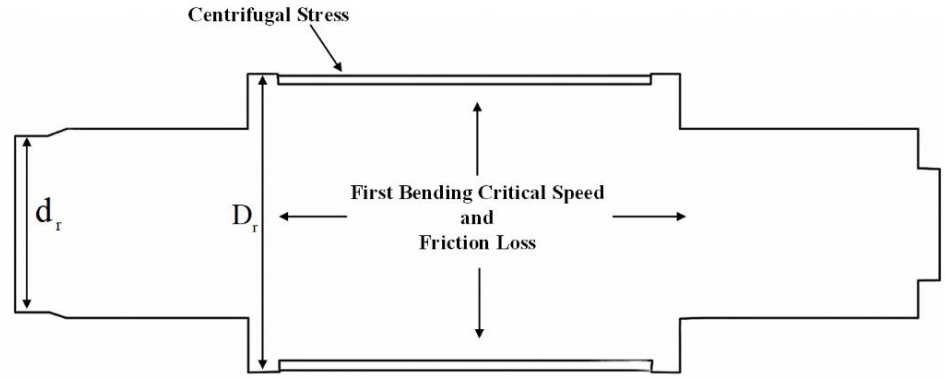


Fig. 5. Rotor mechanical challenges

Critical speed and shaft geometry: According to the nomenclature shown in Fig. 5, the critical rotational speed corresponds to the first bending natural frequency can be determined using the following equation [25]–[27]:

$$n_{cr} = \frac{60}{2\pi} \times \sqrt{\frac{48E\pi d_r^4}{64L^3 m}} \tag{4}$$

In this context, n_{cr} represents the first critical speed, m denotes the rotor mass, L is the rotor length, and d_r is the shaft diameter. To prevent mechanical resonance, the rated speed must be below the first critical speed. In order to shift the first bending mode at speeds above the operating speed, the motor shaft must be short and have a large diameter, i.e., a small L/D_r ratio. It should be noted that equation (4) provides a simplified analytical estimation of the first bending critical speed by modeling the shaft as a simply supported beam, which is commonly used for preliminary analysis of standalone electrical machines. In FESSs, the electrical machine rotor is rigidly coupled to a flywheel inertia rotor with a significantly higher mass and polar moment of inertia. As a result, the first bending critical speed of the coupled EM–flywheel rotor system is substantially lower than that of the electrical machine alone. Therefore, while the general requirement of maintaining the operating speed away from the first bending critical speed remains valid, its realization is considerably more challenging in flywheel applications. In the investigated designs, a hybrid

bearing system consisting of magnetic bearings and mechanical bearings is employed. Mechanical bearings provide structural support and backup functionality, whereas magnetic bearings offer adjustable stiffness and active damping, which strongly affect the rotordynamic characteristics of the coupled rotor system. By appropriate tuning of the magnetic bearing stiffness and control parameters, the critical speed can be shifted away from the operating range or stable operation near or above the first critical speed can be achieved. Consequently, critical speed constraints in flywheel applications must be addressed at the system level, accounting for the combined EM–flywheel rotor and the dynamic behavior of both magnetic and mechanical bearings.

When the rotor speed approaches its critical speed, the rotor and suspension system may experience extreme vibrations or mechanical failure. Rotor dynamics are influenced by various factors such as core length, rotor diameter, bearing stiffness, impeller mass, and gyroscopic effects. To prevent such issues, the maximum operating speed, n_s, must typically be limited by the following equation [28]–[30]:

$$n_s \leq 0.75 n_{cr} \tag{5}$$

The approximate shaft length is determined based on the minimum permissible frequency in relation to the first critical bending speed. For this purpose, the specifications presented in Fig. 6 are used. According to Fig. 6, for a maximum rotor speed, the permissible values of rotor length and diameter are limited to a certain level. For example, based on equation (5), for a nominal speed of 10000 rpm, the value of the first natural frequency must be greater than 13340. Consequently, according to Fig. 6, the allowable values of rotor diameter and length are limited to the blue region. In this case, for the nominal speed of 10000 rpm, the rotor diameter is 212 mm and the length is 286 mm. It should be noted that the effect of core length on critical speed is greater than that of rotor diameter. Furthermore, for a given critical speed, increasing the rotor diameter results in a decrease in core length. Equation (5) represents a simplified analytical expression commonly used for estimating the first bending critical speed of a standalone electrical machine rotor. However, this formulation is not directly applicable when the electrical machine rotor is rigidly coupled to a heavy flywheel inertia rotor, as is the case in FESSs. In practical FESS applications, the large additional mass and polar moment of inertia introduced by the flywheel significantly modify the rotordynamic behavior of the system and lead to a substantially lower first bending critical speed compared to the electrical machine alone. Consequently, the allowable rotor length and shaft geometry cannot be reliably determined using simplified analytical expressions. Instead, these limits have been established through detailed rotordynamic FEA of the coupled EM–flywheel system, taking into account the actual geometry, mass distribution, and the characteristics of both magnetic and mechanical bearings. Accordingly, Eq. (5) is retained in this work only to illustrate general qualitative design tendencies for standalone electrical machines, while all flywheel-related design constraints are enforced through system-level considerations. Fig. 6 is therefore intended to provide a qualitative indication of general trends rather than quantitative design limits for the flywheel application.

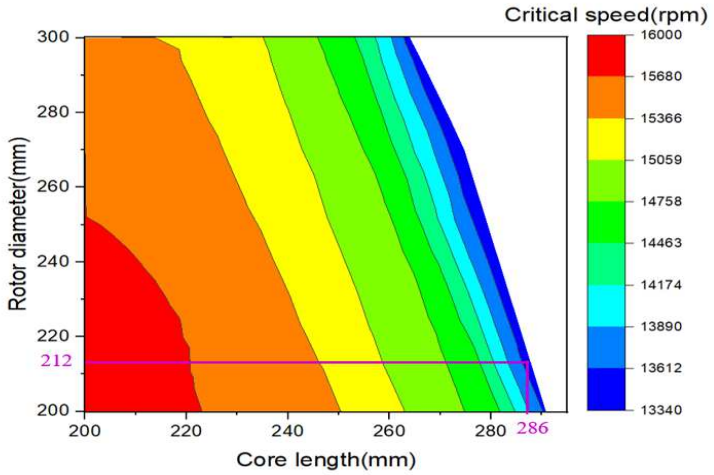


Fig. 6. Allowable core length and rotor diameter considering critical speed constraints

Power-to-rotor volume limitation: The machine internal apparent power S is calculated as:

$$S = C_0 \times A \times B_g \times D^2 \times L \times n_s \quad (6)$$

Where A is the stator electrical loading, B_g is the peak value of the air-gap flux density, and D denotes stator bore diameter. Moreover, the utilization factor C_0 is calculated as follows [28]–[30]:

$$C_0 = \pi^2 \times 1.11 \times k_w \quad (7)$$

Where k_w is the winding factor. In this case, the mechanical output power of the machine P is obtained by:

$$P = (\eta \times \cos\varphi) \times S \quad (8)$$

In which cos φ, and η are the power factor and efficiency, respectively. According to Eqs. (6)-(8), increasing the machine output power requires increasing the machine dimensions, specifically the product of length and the square of the diameter ($L \times D^2$). On the other hand, due to the presence of centrifugal forces and the rotor critical speed limitations, increasing the length and diameter is restricted. To achieve the required output power, either the electrical and magnetic loading must be increased, or the speed must be raised. Taking into account the constraints due to electrical and magnetic loadings, a minimum rotor volume is required for a given power rating, expressed as follows [28]–[30]:

$$P \le C_{mech} L D^2 n_s \quad (9)$$

Where C_{mech} is the mechanical utilization factor.

3.2. Thermal Constraints and Losses

Rotor losses and the effectiveness of the cooling system limit the thermal performance of high-speed electrical machines. Therefore, it is necessary to consider these parameters in the design process as follows:

Rotor loss and cooling limitations: To prevent excessive rotor temperature rise, the maximum allowable rotor loss P_{Rotor} is limited, as given by eq. (10) [23]:

$$P_{Rotor} \le \frac{DL}{\pi \alpha \Delta T} \quad (10)$$

Where α is the convective heat transfer coefficient of the rotor, and ΔT denotes the temperature difference between the rotor surface and the surrounding fluid. Equation (10) was originally formulated for high-speed electrical machines operating under air-cooling conditions, where convective heat transfer plays a significant role. In the context of FESSs, two operating environments were considered in this study: (i) operation at near-atmospheric pressure and (ii) operation under vacuum conditions.

For the non-vacuum case, Equation (10) was applied using conventional values of the convective heat transfer coefficient. For the vacuum-operated flywheel configurations, convective cooling was assumed to be negligible, and the same formulation was employed with a significantly reduced effective heat transfer coefficient (α). In this case, heat removal is dominated by conduction through the hollow shaft, mechanical interfaces, and spray cooling of the shaft, with radiation providing a secondary cooling mechanism.

Rotor windage (air friction) losses: Windage losses increase with rotor speed, rotor surface roughness, and ventilation velocity (i.e., the speed of axial cooling airflow). According to [29], [31], the frictional power P_{fr} resulting from the drag torque opposing the rotation of a cylinder with radius R_r can be approximated as follows:

$$P_{fr} = k_f c_T \rho_{air} \pi \omega^3 R_r^4 l_r \quad (11)$$

Here, ω denotes the angular velocity of the rotor, ρ_{air} is the air-gap density, R_r is the rotor radius, and l_r is the axial length of the slitted section of the rotor. The torque coefficient c_T depends on the tip Reynolds number and must be determined separately for different flow regimes. The surface roughness coefficient k_f is 1.0 for a smooth rotor and approximately 2.5 for a rotor surface with axial slits. According to Eq. (11), the type of fluid surrounding the rotor directly affects the windage losses. Moreover, windage losses vary proportionally to the cube of the rotor's rotational speed; hence, with increasing rotor speed, windage losses increase significantly. For this reason, the rotating components of a FESS, namely, the rotor and the flywheel disk, are enclosed within a

vacuum chamber to minimize windage losses. The effect of vacuum chamber pressure on windage losses in a FESS operating at speeds ranging from 1000 to 30000 rpm is shown in Fig. 7. The analysis is conducted for two pressure levels: 0.01 Pa and 0.1 Pa. The results show that windage losses increase significantly with rising pressure, indicating the necessity of maintaining a high-quality vacuum environment to minimize windage losses. Equation (11) represents a simplified estimation of windage losses and is primarily applicable to rotors operating in atmospheric or near-atmospheric conditions under continuum flow assumptions. It does not explicitly distinguish between disc and drum contributions, nor does it account for additional pumping losses associated with forced or induced cooling airflow. In FESSs operating under vacuum, the flow regime is governed by the Knudsen number, and the underlying physics of windage losses changes significantly. For sufficiently low pressures and high peripheral speeds, the flow transitions from continuum to molecular regime, in which conventional aerodynamic loss formulations are no longer valid. In practical high-speed flywheel systems, particularly composite rotors with tip speeds approaching 800 m/s, operation typically occurs in the molecular flow regime, whereas steel rotors generally operate at lower peripheral speeds. In this study, Equation (11) was employed as a comparative metric rather than an exact loss prediction model.

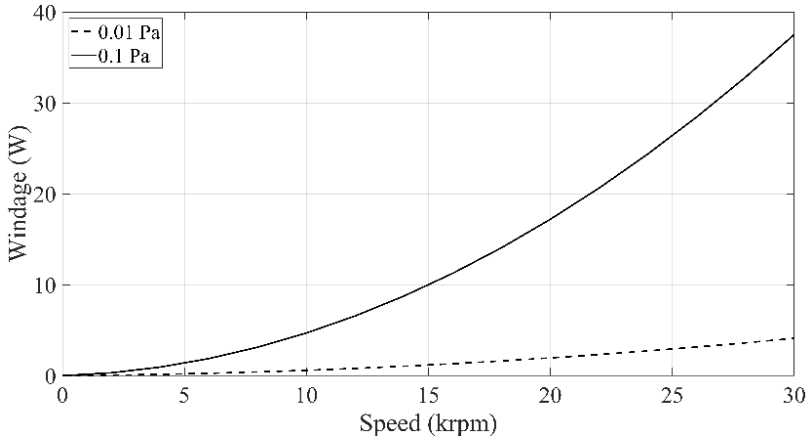


Fig. 7. Effect of vacuum chamber pressure on windage losses

Core losses: The core (iron) losses of an electrical machine can be calculated as follows [29]:

$$P_{fe} = P_h + P_e + P_a = k_h f B_m^2 + k_e f^2 B_m^2 + k_a f^{1.5} B_m^{1.5} \tag{12}$$

Where k_h, k_e, and k_a denote the hysteresis, eddy current, and excess loss coefficients, respectively. These coefficients are material-dependent and are typically considered constant with respect to frequency (f) and peak flux density (B_m). However, under high-speed operating conditions, due to the non-sinusoidal nature of the magnetic flux waveform in the iron core, the eddy current loss coefficient exhibits a dependency on frequency. As is clear, increasing the supply frequency in high-speed machines leads to increased core losses. In high-speed machines, core losses are minimized by employing soft magnetic materials with low specific core loss and thin laminations.

3.3. Electrical and Magnetic Loading Constraints

Magnetic loading directly affects the induced voltage in the armature windings and the core losses of the machine. In AC machines, the induced voltage in the armature windings is calculated as follows [28]–[30]:

$$E_{rms} = 4.44 \times N_s \times f \times B_{avg} \times A_p \times k_w \tag{13}$$

Where E_{rms}, N_s, B_{avg}, and A_p are the RMS value of induced voltage, the number of turns per phase in the winding, the average air-gap flux density, and the effective cross-sectional area of the magnetic flux per pole, respectively. In high-speed machine design, increasing rotor speed leads to an increase in the RMS value of the induced voltage. This phenomenon can pose a critical design challenge, particularly in PMSMs operating under no-load or light-load conditions, as it may increase the risk of magnetic saturation and result in higher core losses. Moreover, as previously discussed, high magnetic loading significantly increases core

losses in the machine. During the design process, it is necessary to select the values of magnetic loadings and air-gap flux density by taking into account the core loss limitations and temperature constraints of various machine components. Typical flux density and current density values for various machine components used in low- and high-speed machine designs are presented in Table 1. In addition, magnetic loading values in relation to the power rating and rotational speed of electrical motors are illustrated in Fig. 8. As shown, both magnetic and electrical loading levels are significantly lower in high-speed machines compared to their low-speed counterparts [32], [33].

Table 1. Typical magnetic and electrical loading values

Items		Low-Speed Machine	High-Speed Machine
Flux Density [T]	Stator Teeth	1.4 – 2.1	1.1 – 1.4
	Stator Yoke	1.3 – 1.7	0.8 – 1.2
	Rotor Teeth	1.5 – 2.2	1.0 – 1.5
	Rotor Yoke	0.5 – 1.5	0.4 – 1.5
	Air-gap	0.5 – 0.9	0.3 – 0.7
Current Density [A/mm^2]	Stator Winding	3.0 – 8.0	3.0 – 5.0
	Rotor Bar	3.0 – 8.0	8.0 – 16.0
	Rotor End-ring	3.0 – 7.0	8.0 – 15.0

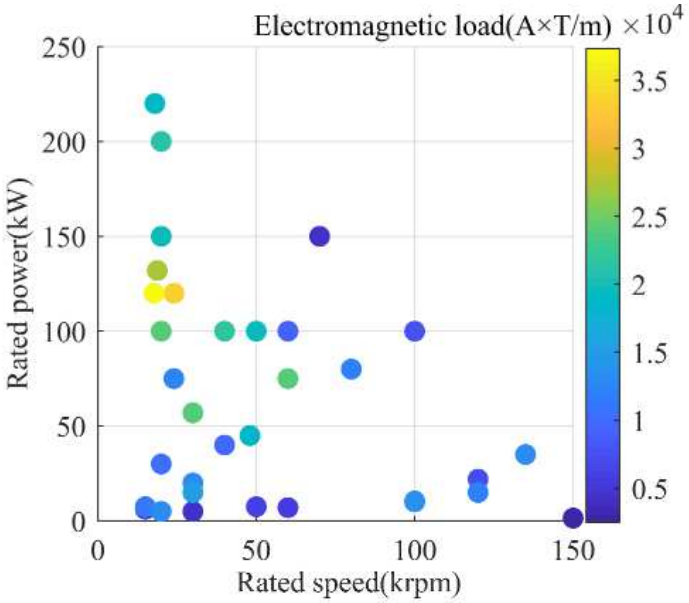


Fig. 8. Magnetic loading values with respect to power rating and rotational speed in electrical motors [34]

3.4. Integrated Design Algorithm

The mechanical, thermal, magnetic, and electrical constraints presented above form the basis of the proposed algorithmic framework presented in this section. In particular, the mechanical (centrifugal forces, rotor critical speed limitation, …), thermal (loss generation, temperature rise, and cooling capability), magnetic (flux density limits, saturation, and demagnetization risk), and electrical (efficiency, torque ripple, and power factor) constraints are explicitly incorporated into the different steps of the design algorithm. Fig. 9 illustrates the design flowchart of the thirteen studied electrical machines. As shown, the electrical machine design procedure consists of the following steps:

Step 1: Perform the analytical design while considering magnetic, mechanical, and thermal constraints within the specified power and speed range. In this stage, the main dimensions and electromagnetic parameters of each electrical machine — including

stator inner and outer diameters, axial length of the core, slot geometry, air-gap length, and rotor geometry — are determined using Eqs. (1)–(13), the allowable limits summarized in Table 1 and Fig. 8, and FE-based estimations.

Step 2: Evaluate the analytical design with the help of analytical methods to confirm its accuracy. If necessary, repeat the design process iteratively until the desired performance specifications are attained.

Step 3: After confirming the initial analytical design, a detailed FE model of the motor is developed and evaluated. The flux density distribution, electrical and magnetic loadings obtained from the FE model are compared with the permissible values presented in Table 1 and Fig. 8 to ensure that all magnetic, thermal, and electrical limits are satisfied. This step ensures consistency between the analytical design and the multiphysics constraints introduced in section 3.

Step 4: A sensitivity analysis is conducted on the FE-simulated electrical machine, and design parameters are adjusted to achieve optimal output characteristics.

Step 5: Analyze and extract technical indicators, such as efficiency, power factor, and torque ripple as well as economic indicators.

This five-step design process was applied to all thirteen electrical machines under study. For each machine type, the flowchart in Fig. 9 was iteratively followed until optimal output characteristics were achieved.

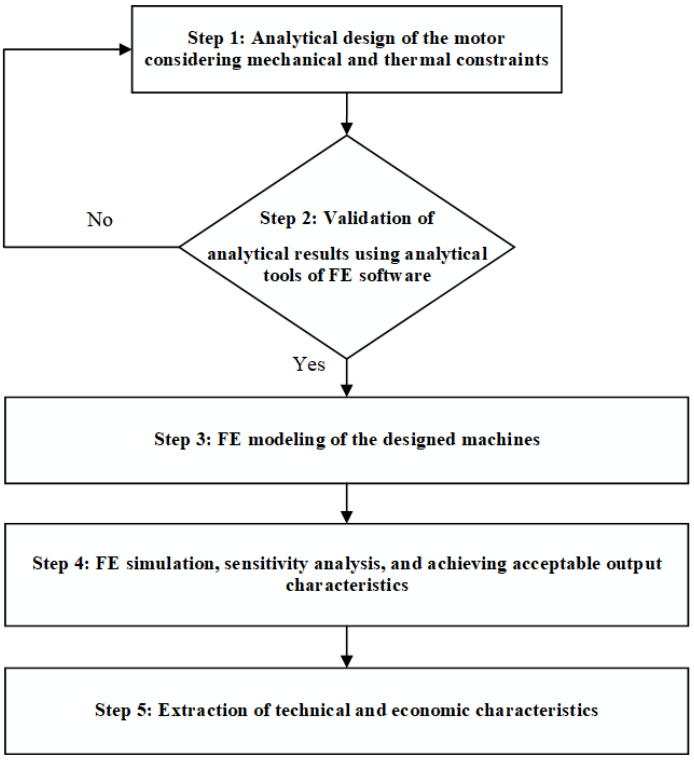


Fig. 9. Design flowchart of the studied electrical machines

Changing the electrical machine type alters the rotor weight (the axial load on the magnetic suspension system) and affects the loss distributions within both the electrical machine and the suspension system. These changes significantly affect the temperature distribution of the electrical machine. Therefore, to consider interactions between the electrical machine and other components (such as the suspension and cooling systems), these components—particularly the cooling system—have been reanalyzed and redesigned. This process has been carried out for each of the thirteen electrical machine types studied in this paper. For this purpose, the comprehensive flowchart shown in Fig. 10 is proposed. As illustrated in this figure, the various stages of this process are as follows:

Stage 1: Selection of the basic configuration of the FESS, including the mechanical connection method and placement of its components (The structure shown in Fig. 3).

Stage 2: Magnetic design of the electrical machine (as shown in the flowchart of Fig. 9), including the estimation of losses in

various components and calculation of the rotor and shaft assembly weight.

Stage 3: Design of the rotating mass of the FESS and determination of its weight based on the required energy capacity, while considering mechanical constraints. In this stage, minimizing the rotating mass weight to meet the required energy capacity is defined as the objective function.

Stage 4: Design and simulation of the active radial and passive axial magnetic bearings, along with the calculation of magnetic bearing losses using FE software.

Stage 5: Thermal modeling of the electrical machine and magnetic bearings, along with cooling system design using FE software. In this stage, based on the magnetic simulations of the electrical machine and magnetic bearings from stages 2 and 4 and the obtained loss values (including magnetic, joule, and mechanical losses), the loss sources in the thermal model are updated. After solving the thermal model, temperatures at various parts of the electrical machine and magnetic bearings are evaluated. Note that the thermal boundary conditions, cooling system configurations, and heat transfer parameters used in this study were chosen from published experimental and numerical studies of high-speed electrical machines and FESSs documented in the literature. For housing water jacket cooling systems, the modeling technique, parameters of the cooling system, and design recommendations were taken from the studies described in [35]–[46]. For spray cooling systems, the implementation method and cooling characteristics were taken from [37], [38], [47], [48]. Likewise, the shaft spiral groove cooling configuration and corresponding thermal parameters were determined using the methodologies presented in [37], [38], [49]–[51]. These references were used not only for determining the settings of cooling system and thermal boundary conditions, but also as a benchmark to validate that the predicted temperature distributions remained within the ranges reported for similar machine topologies and operating conditions. If the temperatures are within the allowable range, the simulation terminates. However, if the temperatures of critical components—such as conductors, stator core, rotor core, etc.—exceed permissible limits, three scenarios will be implemented to reduce the temperature:

Scenario 1: Return to stage 2 and repeat the electrical machine magnetic design algorithm with the goal of reducing losses and consequently reducing the temperature of critical points in the machine.

Scenario 2: Improving the cooling process by employing more advanced and combined cooling techniques. In the case of FESSs that operate under vacuum conditions, convective heat transfer is negligible and is not considered in the thermal analysis. In such cases, the heat generated is removed by conduction through the hollow shaft, mechanical interfaces, and spray cooling of the shaft, with radiation providing a secondary cooling mechanism. Then, heat can be removed by external cooling systems located outside the vacuum enclosure.

Scenario 3: High-temperature design of the electrical machine using materials with higher thermal tolerance, followed by returning to stage 2 to repeat the simulation process. For example, in PM machines, replacing NdFeB magnets with SmCo magnets increases the thermal tolerance of the rotor magnets. In such cases, the design process must be restarted from stage 2.

Stages 1 through 5 are repeated for each of the thirteen different types of electrical machines until an acceptable thermal performance is achieved. Upon validation of the machine's thermal behavior, the design process is concluded, and all performance characteristics of the electrical machine—including efficiency, power factor, volume and mass, torque ripple, cost, and others—are extracted.

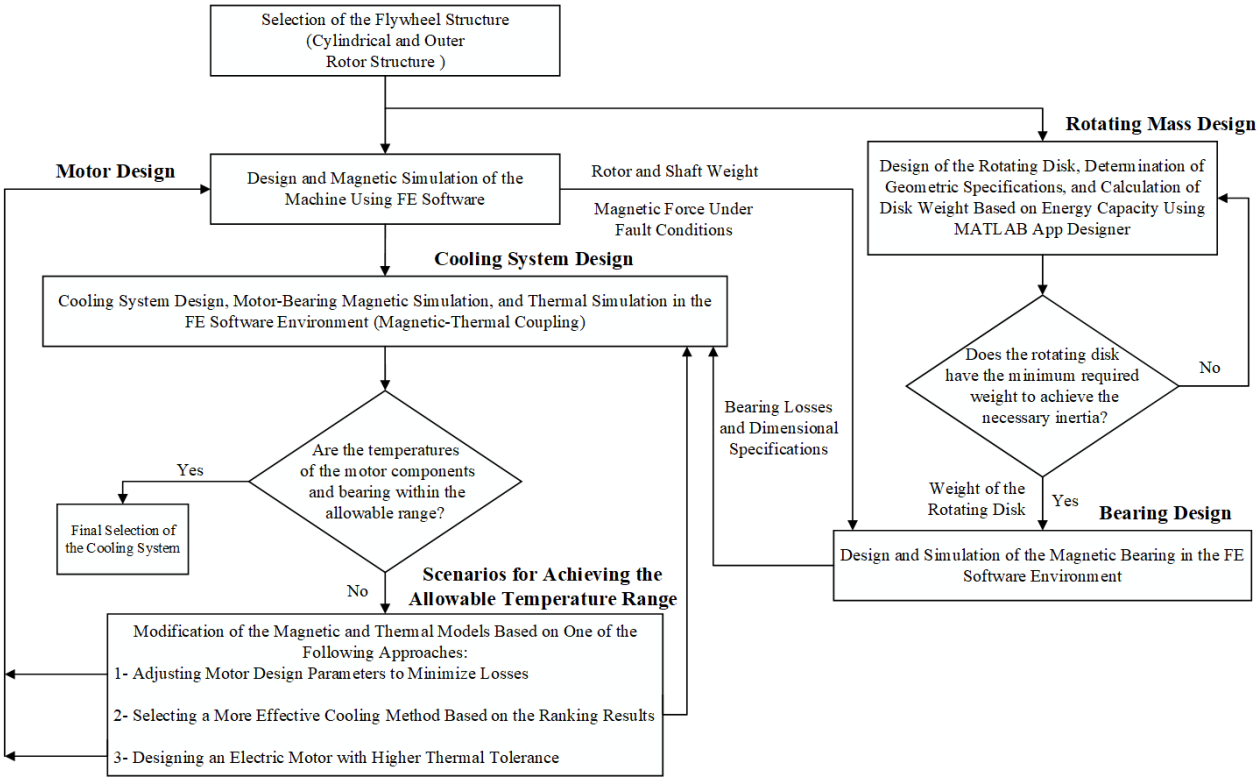


Fig. 10. Flowchart illustrating the design, modeling, and simulation of the electrical machine, considering its interaction with other components in the FESS

This integrated design framework provides a systematic approach to design the electrical machines for flywheel applications, ensuring that all mechanical, thermal, magnetic, and electrical constraints are met. In section 4, the application of this framework to 13 specific machine topologies is presented.

4. Description of 13 Machine Topologies and Design Assumptions

In this section, the thirteen electrical machine topologies chosen for evaluation in this study, along with their design assumptions and material specifications, are introduced. Various types of electrical machines have been investigated in the literature for use in FESS, and some of them have been implemented in commercialized products. The selection of appropriate machine types for FESS remains a persistent design challenge, as this choice directly impacts both the system's performance characteristics and cost metrics. For this purpose, analytical design and detailed FEA-based simulations are conducted for thirteen different machine topologies. All machines are designed for a FESS with a rated power of 100 kW, an energy capacity of 10 kWh, a rotational speed of 10000 rpm, and a terminal voltage of 400 V. It should be mentioned that in the design process of each type of electrical machine, magnetic, mechanical, and thermal limitations (topics discussed in previous sections) are considered. In FESSs, the electrical machine operates over a wide speed range determined by the minimum and maximum allowable rotor speeds. Accordingly, each machine topology was evaluated at two representative operating points: the maximum speed condition, corresponding to rated power operation, and a minimum speed condition assumed to be half of the maximum speed. At the minimum speed, the required electromagnetic torque is constant while the power is reduced by half. The overall performance indicators were obtained by considering both cases, providing a representative assessment of machine behavior over the full operating speed range of the flywheel. After simulating the electrical machines and calculating the technical and economic indicators, the optimal machine topology used in the FESS is selected based on the multi-criteria decision-making (MCDM) method. Accordingly, the completion of the decision-making table is not based on the scattered data presented in the references but on the results obtained from the design and simulation of the FEA of electrical machines under the same conditions for the types of motors. Table 2 presents the

various types of electrical machines studied in this paper. In order to evaluate these types of electrical machines under the same conditions, the materials of similar parts in different machines are considered the same, as detailed in Table 3. As previously presented, the main sub-components of the FESS include the electrical machine, the suspension system, the rotating mass, and the cooling system. Therefore, to evaluate the performance characteristics of the FESS at the system level under the influence of selecting different types of electrical machines, the design of the electrical machine is considered. Additionally, the suspension system and cooling system are also designed in this paper. Finally, a summary of the results is presented. In this paper, the main focus is on the design of the electrical machine part and the evaluation of its technical and economic indicators. The FEA simulations in section 5 are based on the thirteen topologies described in this section, with the material specifications and design assumptions. The performance indicators extracted from these simulations are used in the TOPSIS analysis in section 6.

Table 2. Structures of the studied machines for FESS applications

Number	Structure
1	2-pole surface-mounted permanent magnet motor (2PSMPMM)
2	4-pole surface-mounted permanent magnet motor (4PSMPMM)
3	2-pole interior permanent magnet motor (2PIPMM)
4	4-pole interior permanent magnet motor (4PIPMM)
5	2-pole Synchronous reluctance motor (2PSRM)
6	4-pole Synchronous reluctance motor (4PSRM)
7	2-pole permanent magnet-assisted synchronous reluctance motor (2PPMASRM)
8	4-pole permanent magnet-assisted synchronous reluctance motor (4PPMASRM)
9	Switched Reluctance motor (SRM)
10	Solid rotor induction motor (SoRIM)
11	Slitted rotor induction motor (SlRIM)
12	Copper coated solid rotor induction motor (CCSoRIM)
13	Copper coated slitted rotor induction motor (CCSlRIM)

Table 3. Materials used for each part of the designed machine

Part	Material	Maximum Allowable Operating Temperature (°C)
Stator core	JEF Steel /20JNHF 1300	200
Rotor core	JEF Steel /10JNHF 600	200
Permanent magnet	N35UH (NdFeB)	180
Winding	Copper	155
Sleeve	Inconel 718	700
Shaft	Stainless Steel 316	200

5. FEA and Performance Results

In this section, the FEA simulation results for the thirteen machine topologies introduced in section 4 are presented. The results include the magnetic flux distribution, torque characteristics, loss distribution, and thermal behavior. In addition, a mesh convergence study and validation against analytical predictions are provided to verify the exactness of the numerical models. The duty cycle is defined as the relative proportion of time during which the flywheel actively exchanges power (charging or discharging) compared to the time spent in idle or standby operation at high rotational speed. Depending on the load profile and thermal behavior, the operating conditions of electrical machines can be classified into several duty types (S1–S10) (IEC 60034-1). The operating profile of the FESS for frequency control is inherently stochastic and determined by the actual grid frequency deviations and load fluctuations in real time. Therefore, the charge/discharge pattern and standby duration cannot be predetermined deterministically. From the IEC classification point of view, this application can be represented by duty type S9, which corresponds

to operation with non-periodic load and speed variations, including frequent overloads. Because the demand for grid frequency regulation is stochastic and depends on the system, a fixed numerical duty cycle percentage is not a good way to describe the operating conditions. For the electric vehicle application, the flywheel is used in acceleration (discharge mode) and regenerative braking (charge mode), with occasional rest periods, which matches IEC duty types S4 (intermittent periodic duty with starting) and S5 (intermittent periodic duty with electric braking). However, similar to the frequency control case, the precise duty cycle depends on the driving cycle (urban, highway, aggressive, mild driving patterns). Since driving cycles are not uniquely defined and vary significantly, a single fixed numerical duty cycle would be arbitrary and misleading. The thirteen different types of electrical machines have been designed and simulated and their important performance characteristcs have been extracted using FEA. First, to confirm the numerical model, a quantitative comparison between results of analytical predictions and FE has carried out for three machine topologies. The obtained results are summarized in Table 4. The maximum error between results of analytical calculations and FEA is less than 5%. Therefore, the validity of the analytical design procedure and providing additional confidence in the numerical results presented in this section is confirmed. It should be mentioned that the preliminary design values were attained either from the analytical sizing technique developed in this work or from the analytical/preliminary design tools embedded in commercial machine-design software, depending on the machine topology. Furthermore, a mesh convergence study has performed to confirm that the attained results are independent of mesh density and the results are given in Table 5. As observed, the obtained results show slight difference between the two finest meshes (80000 and 100000 elements). Thus, an adaptive mesh comprising about 80000 elements is adopted for all subsequent simulations.

Table 4. Comparison between analytical predictions and FEA results for representative topologies

	Efficiency			Torque Density			Power Factor		
Machine Type	Analytical (%)	FEA (%)	Error (%)	Analytical (Nm/kg)	FEA (Nm/kg)	Error (%)	Analytical	FEA	Error (%)
4PIPMM	96.2	95.1	1.14	1.24	1.2	3.23	0.97	0.94	3.09
4PSMPMM	97.4	96.8	0.62	1.55	1.50	3.23	0.98	0.95	3.06
SIRIM	96.8	96	0.83	0.74	0.71	4.05	0.89	0.86	3.37

Table 5. Mesh convergence study for the 4PSMPMM topology

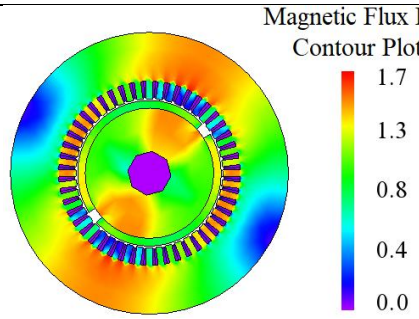
Number of Elements	Efficiency (%)	Torque Density (Nm/kg)	Power Factor
30000	96.52	1.487	0.946
50000	96.71	1.495	0.949
80000	96.79	1.499	0.95
100000	96.81	1.5	0.95

Fig. 11 presents the results of the magnetic and thermal simulations for the thirteen different types of electrical machines. As observed, the machines have been designed to deliver an output power of 100 kW at a rated speed of 10000 rpm. The flywheel's rotational speed has a significant impact on the available output power in FESSs; lower speeds lead to lower power capability. The comparative analysis and selection of electrical machine topologies that can meet the necessary power transfer over the flywheel's entire speed range are the main goals of the suggested design framework. In order to ensure viability under reduced-speed conditions, machine performance is assessed at both maximum and minimum rotational speeds. Future research is directed toward a comprehensive optimization of flywheel energy capacity in relation to its power characteristics, which would necessitate an integrated system-level design approach.

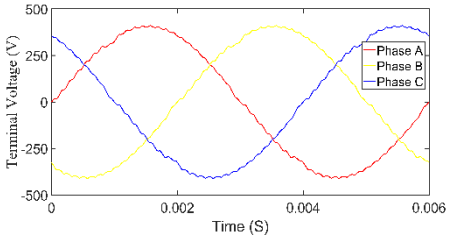
During the magnetic design process, the maximum flux density in key motor components—such as the stator teeth, stator yoke, and rotor—was evaluated. Where necessary, design parameters were adjusted to ensure that flux density levels remain within acceptable limits.

One of the main challenges in designing the cooling system for the electrical machine used in FESS is maintaining the rotor temperature within the allowable thermal range. As previously discussed, to reduce windage losses, the rotor operates under vacuum conditions. Since heat transfer from the rotor to the stator is not possible in a vacuum, even small amounts of rotor loss can lead to a significant temperature rise. As a result, rotor cooling remains one of the major design challenges in vacuum-enclosed FESSs. Furthermore, replacing ball bearings with magnetic bearings eliminates conductive heat transfer between the rotor and the outer housing of the motor, further complicating the rotor cooling process. The use of a vacuum pump and magnetic bearings eliminates heat sources associated with windage and frictional losses. However, heat transfer between the rotor and the motor's outer casing faces serious challenges. Due to the large number of simulation results, the thermal analysis is presented in detail only for the 2-pole surface-mounted permanent magnet motor (2PSMPMM). For other machines, only the maximum temperatures of their critical points are presented in numerical form. As shown in Fig. 11, more advanced cooling techniques have been employed to maintain rotor temperatures within acceptable limits in some electrical machines. For example, spray cooling method has been implemented for 4-pole permanent magnet-assisted synchronous reluctance motor (4PPMASRM), and shaft spiral groove and spray cooling methods for solid rotor induction motor (SoRIM). It should be noted that the coolant in the studied flywheel electrical machines is sprayed directly onto the rotor and shaft surface, and heat removal takes place by solid–liquid contact and phase-change mechanisms (local evaporation or boiling at the rotor surface), rather than by convective heat transfer to a surrounding medium, and hence does not require the ambient gas and can function under vacuum conditions. The cooling fluid is injected onto the surface of the rotor, locally absorbs heat, and is then collected and recirculated. Although this method has high local heat flux removal capability, it is mechanically difficult at high rotational speeds because of the sealing, fluid management, and dynamic constraints, so its use is limited to cases with high rotor loss density and is supplemented by conductive heat transfer through the shaft and by loss minimization through electromagnetic design. One of the key factors affecting the thermal behavior and cooling system complexity in electrical machines used in FESS is the distribution of losses across different machine components. Fig. 11 illustrates the loss distribution within the stator and rotor parts of the designed machines. Naturally, higher concentration of losses in the rotor section increases cooling system complexity, which may raise cooling costs. The predicted component temperatures and the allowable operating temperatures of the selected materials presented in Table 3 are compared, and it is confirmed that all investigated machine topologies operate within acceptable thermal limits. It should be noted that the full geometric dimensions, thermal model parameters, and cooling system specifications of all studied machines are provided in the Supplementary Material to this article. These data are made available to facilitate reproducibility and independent verification of the presented results. The performance indicators obtained from the magnetic and thermal FE simulations form the decision matrix for the TOPSIS analysis presented in section 6.

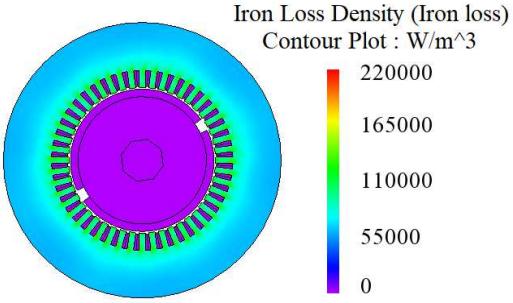
2-pole surface-mounted permanent magnet motor (2PSMPMM)



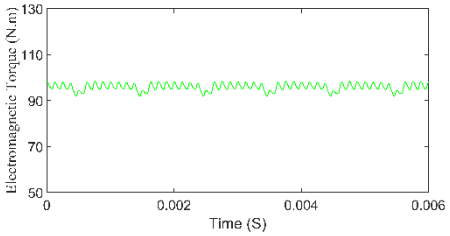
Flux density distribution



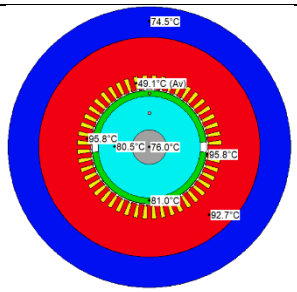
Terminal Voltage (V)

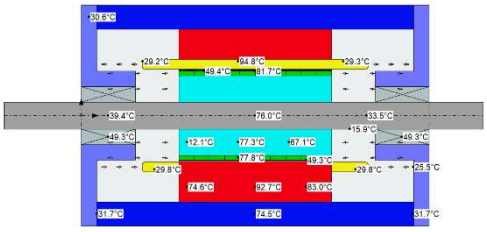


Iron loss distribution



Electromagnetic torque (N.m)



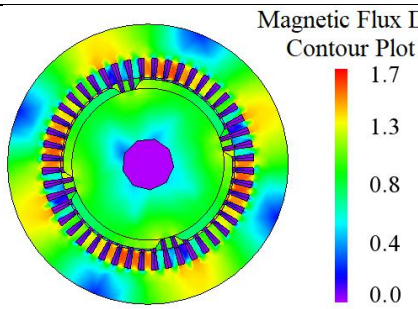


Cooling system: Spray Cooling

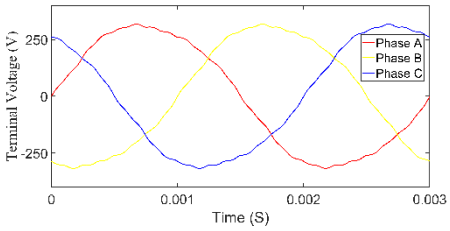
Losses (W): PMs: 4.3 Rotor Banding: 34.7 Rotor Core: 39.4 Stator Core: 2642.8 Stator Windings: 2584.6 Windage: 7.5 Bearings: 800

Temperatures (°C): PMs: 84 Rotor Core: 83.3 Shaft: 78.8 Stator Yoke: 92.8 Stator Tooth: 96 Windings: 96.3

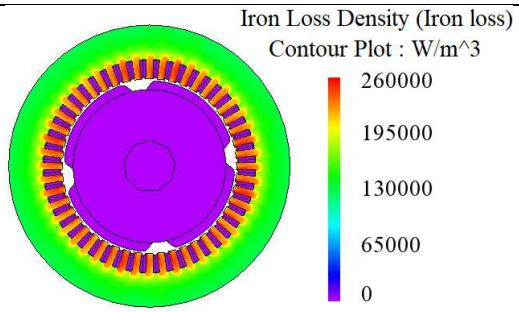
4-pole surface-mounted permanent magnet motor (4PSMPMM)



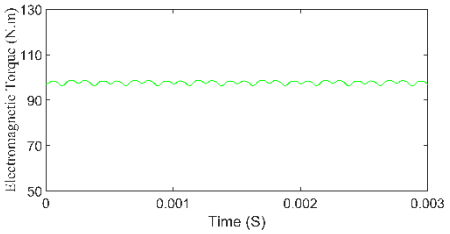
Flux density distribution



Terminal Voltage (V)



Iron loss distribution



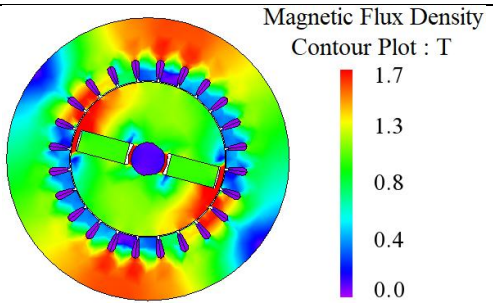
Electromagnetic torque (N.m)

Cooling system: Housing Water Jacket

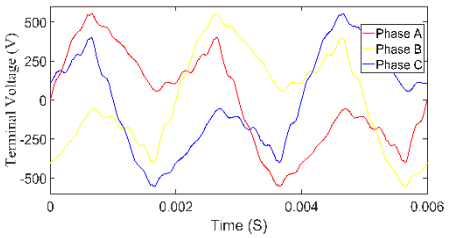
Losses (W): PMs: 4.75 Rotor Banding: 68.3 Rotor Core: 1.3 Stator Core: 1853 Stator Windings: 1533 Windage: 7.5 Bearings: 800

Temperatures (°C): PMs: 79.2 Rotor Core: 79.3 Shaft: 79.4 Stator Yoke: 32.3 Stator Tooth: 37.8 Windings: 68.5

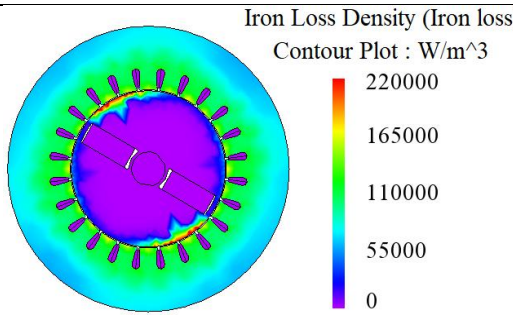
2-pole interior permanent magnet motor (2PIPMM)



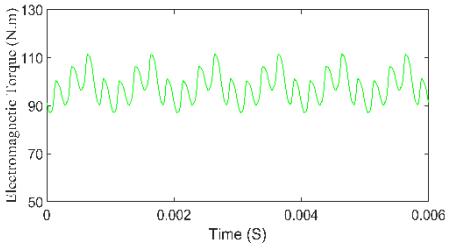
Flux density distribution



Terminal Voltage (V)



Iron loss distribution



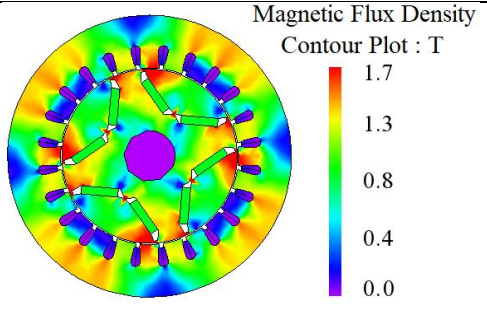
Electromagnetic torque (N.m)

Cooling system: Housing Water Jacket

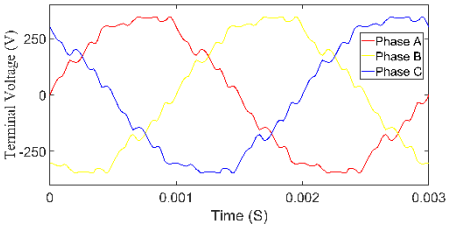
Losses (W): PMs: 161.1 Rotor Core: 60.74 Stator Core: 7365 Stator Windings: 1148 Windage: 7.5 Bearings: 800

Temperatures (°C): PMs: 127.7 Rotor Core: 127.8 Shaft: 127.8 Stator Yoke: 81.6 Stator Tooth: 89 Windings: 91.8

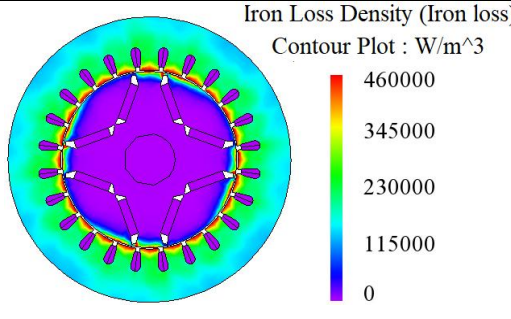
4-pole interior permanent magnet motor (4PIPMM)



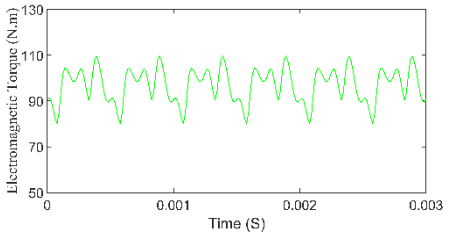
Flux density distribution



Terminal Voltage (V)



Iron loss distribution



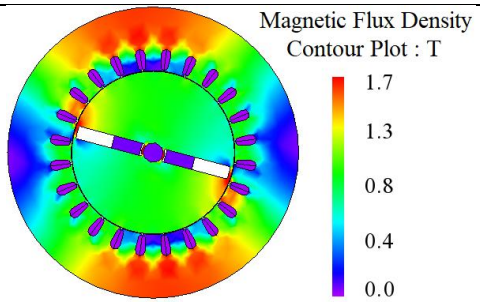
Electromagnetic torque (N.m)

Cooling system: Housing Water Jacket

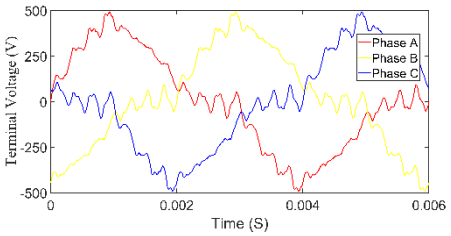
Losses (W): PMs: 175.4 Rotor Core: 4.5 Stator Core: 2598 Stator Windings: 1046 Windage: 7.5 Bearings: 800

Temperatures (°C): PMs: 135.5 Rotor Core: 135.6 Shaft: 135.2 Stator Yoke: 69.8 Stator Tooth: 74.8 Windings: 78.6

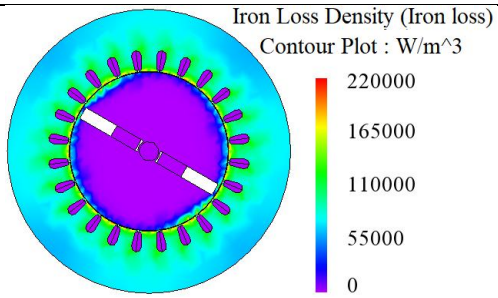
2-pole Synchronous reluctance motor (2PSRM)



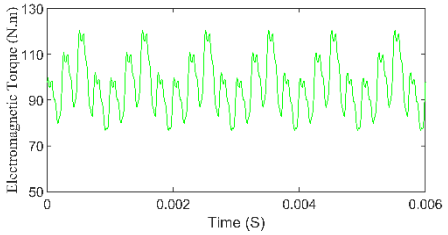
Flux density distribution



Terminal Voltage (V)



Iron loss distribution



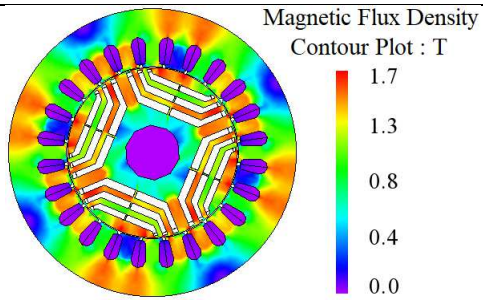
Electromagnetic torque (N.m)

Cooling system: Housing Water Jacket

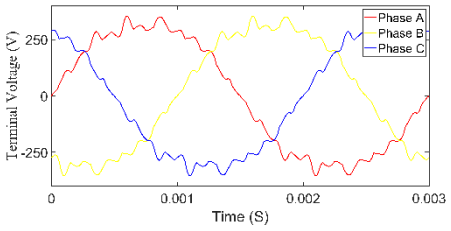
Losses (W): Rotor Core: 128.9 Stator Core: 3267 Stator Windings: 591 Windage: 7.5 Bearings: 800

Temperatures (°C): Rotor Core: 95.8 Shaft: 95.7 Stator Yoke: 67.4 Stator Tooth: 71.1 Windings: 71.9

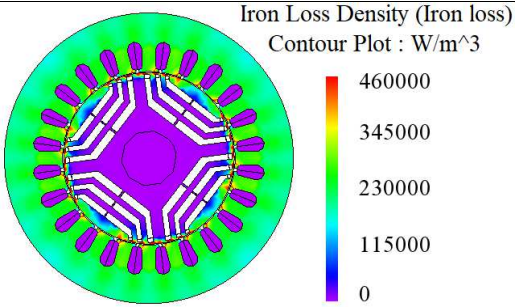
4-pole Synchronous reluctance motor (4PSRM)



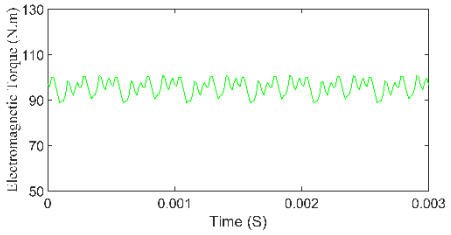
Flux density distribution



Terminal Voltage (V)



Iron loss distribution



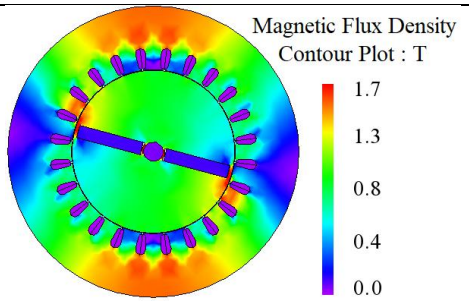
Electromagnetic torque (N.m)

Cooling system: Shaft Spiral Groove and Spray Cooling

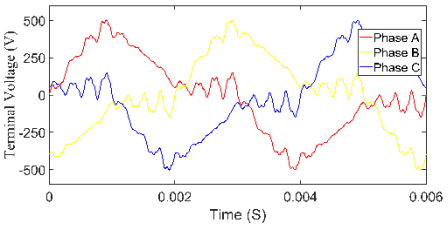
Losses (W): Rotor Core: 4.96 Stator Core: 5450 Stator Windings: 800 Windage: 7.5 Bearings: 800

Temperatures (°C): Rotor Core: 48.1 Shaft: 12.5 Stator Yoke: 86.6 Stator Tooth: 86.6 Windings: 50.1

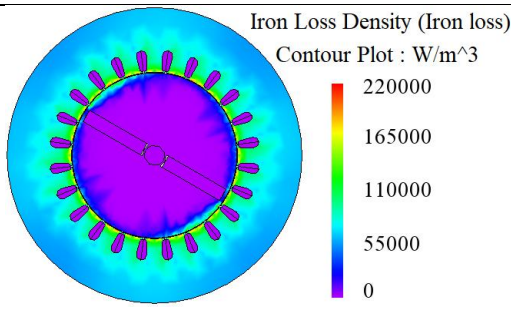
2-pole permanent magnet-assisted synchronous reluctance motor (2PPMASRM)



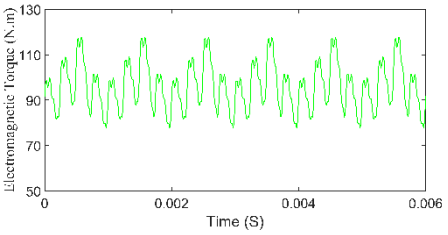
Flux density distribution



Terminal Voltage (V)



Iron loss distribution



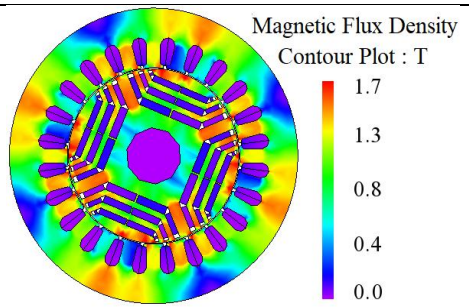
Electromagnetic torque (N.m)

Cooling system: Housing Water Jacket

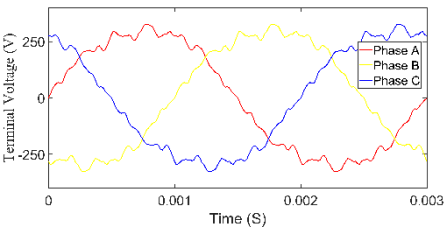
Losses (W): PMs: 130.5 Rotor Core: 96.9 Stator Core: 3051 Stator Windings: 436.5 Windage: 7.5 Bearings: 800

Temperatures (°C): PMs: 79.6 Rotor Core: 80.3 Shaft: 80.3 Stator Yoke: 56.1 Stator Tooth: 59.4 Windings: 59.8

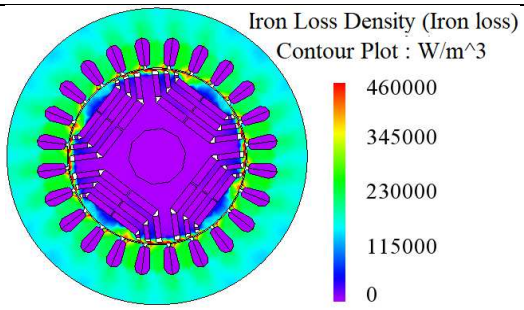
4-pole permanent magnet-assisted synchronous reluctance motor (4PPMASRM)



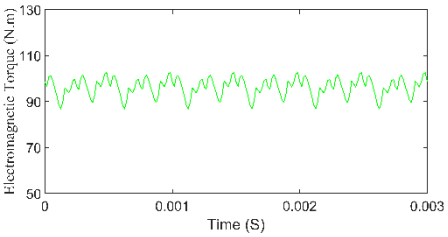
Flux density distribution



Terminal Voltage (V)



Iron loss distribution



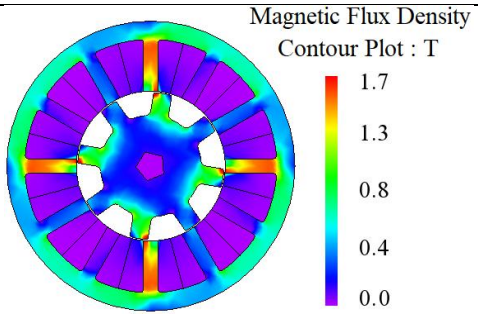
Electromagnetic torque (N.m)

Cooling system: Spray Cooling

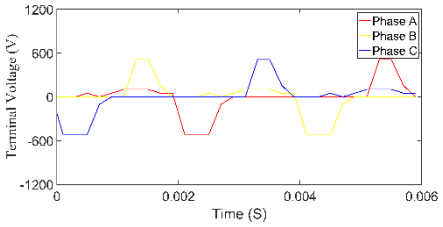
Losses (W): PMs: 240.2 Rotor Core: 5.2 Stator Core: 4519 Stator Windings: 620.8 Windage: 7.5 Bearings: 800

Temperatures (°C): PMs: 75.2 Rotor Core: 67.3 Shaft: 52.5 Stator Yoke: 105.5 Stator Tooth: 99.2 Windings: 40

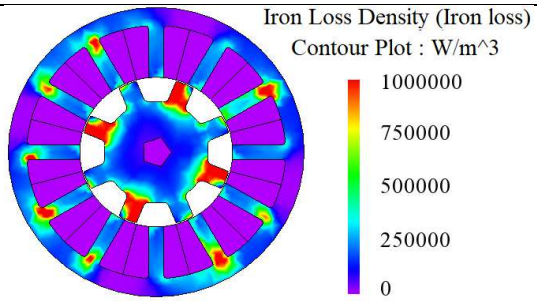
Switched Reluctance motor (SRM)



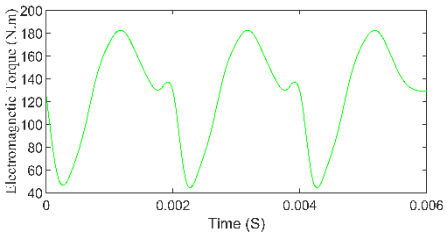
Flux density distribution



Terminal Voltage (V)



Iron loss distribution



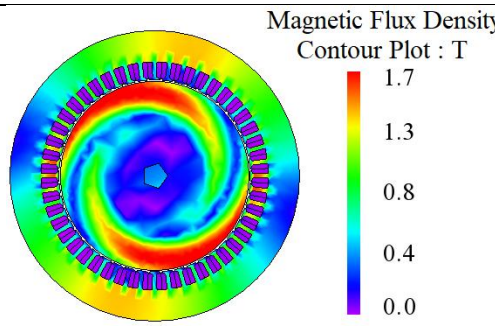
Electromagnetic torque (N.m)

Cooling system: Shaft Spiral Groove and Spray Cooling

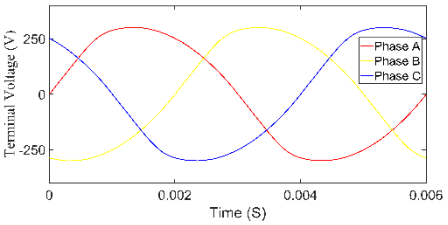
Losses (W): Rotor Core: 407 Stator Core: 2561 Stator Windings: 836.9 Windage: 7.5 Bearings: 800

Temperatures (°C): Rotor Yoke: 84.4 Rotor Pole: 84.7 Shaft: 22.9 Stator Yoke: 86.3 Stator Tooth: 87 Windings: 80.4

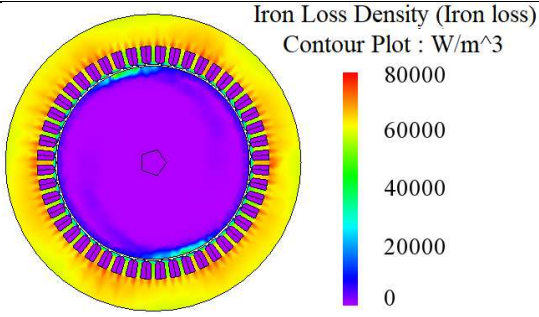
Solid rotor induction motor (SoRIM)



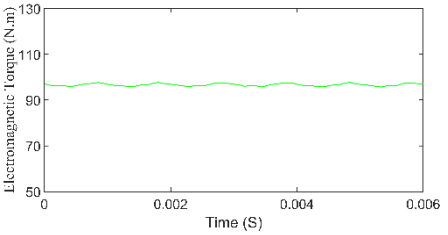
Flux density distribution



Terminal Voltage (V)



Iron loss distribution



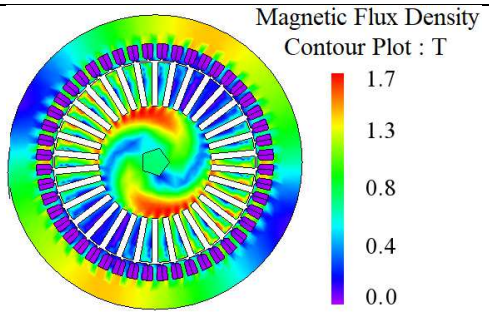
Electromagnetic torque (N.m)

Cooling system: Shaft Spiral Groove and Spray Cooling

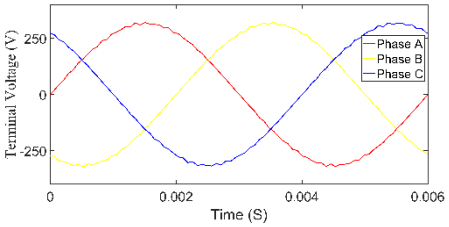
Losses (W): Rotor Core: 3946 Stator Core: 497 Stator Windings: 1122 Windage: 250 Bearings: 800

Temperatures (°C): Rotor Yoke: 186.2 Shaft: 37.2 Stator Yoke: 52.4 Stator Tooth: 185.8 Windings: 59.9

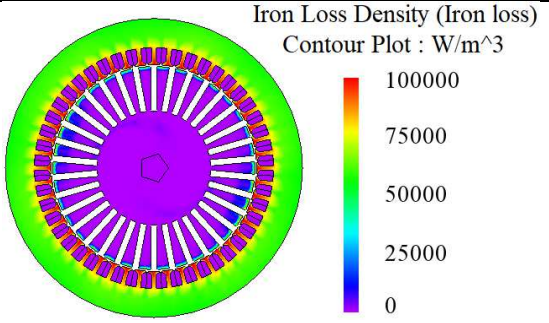
Slitted rotor induction motor (SlRIM)



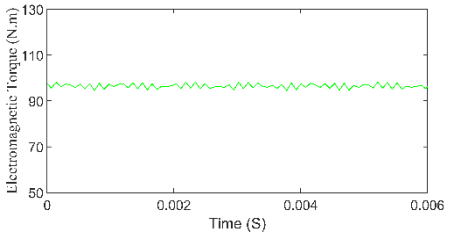
Flux density distribution



Terminal Voltage (V)



Iron loss distribution



Electromagnetic torque (N.m)

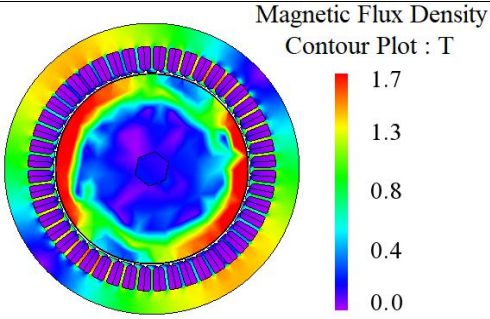
Cooling system: Housing Water Jacket

Losses (W): Rotor Core: 2124 Stator Core: 504 Stator Windings: 1024 Windage: 268 Bearings: 800

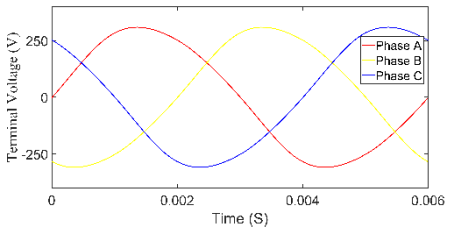
Temperatures (°C): Rotor Yoke: 157.7 Rotor Tooth: 144.5 Rotor Bar: 144.5 Shaft: 155.1 Stator Yoke: 21.7

Stator Tooth: 34.5 Windings: 35.1

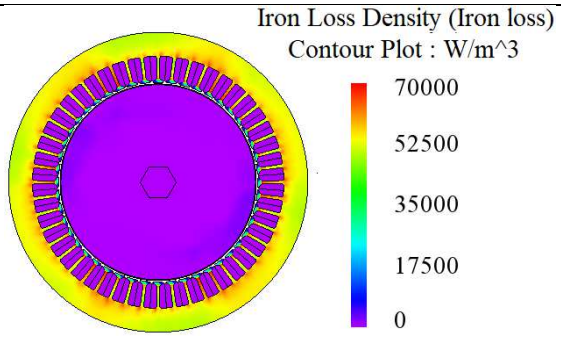
Copper coated solid rotor induction motor (CCSoRIM)



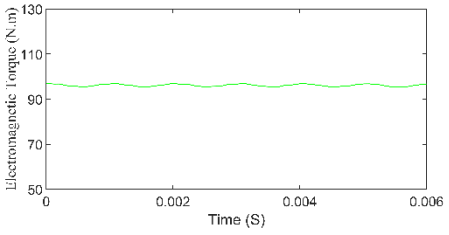
Flux density distribution



Terminal Voltage (V)



Iron loss distribution



Electromagnetic torque (N.m)

Cooling system: Housing Water Jacket

Losses (W): Rotor Copper: 2519 Rotor Core: 487 Stator Core: 232.6 Stator Windings: 1516 Windage: 280 Bearings: 800

Temperatures (°C): Rotor Yoke: 184.2 Rotor Tooth: 184.1 Copper Coating: 184.1 Shaft: 168.2 Stator Yoke: 22

Stator Tooth: 51.9 Windings: 54.2

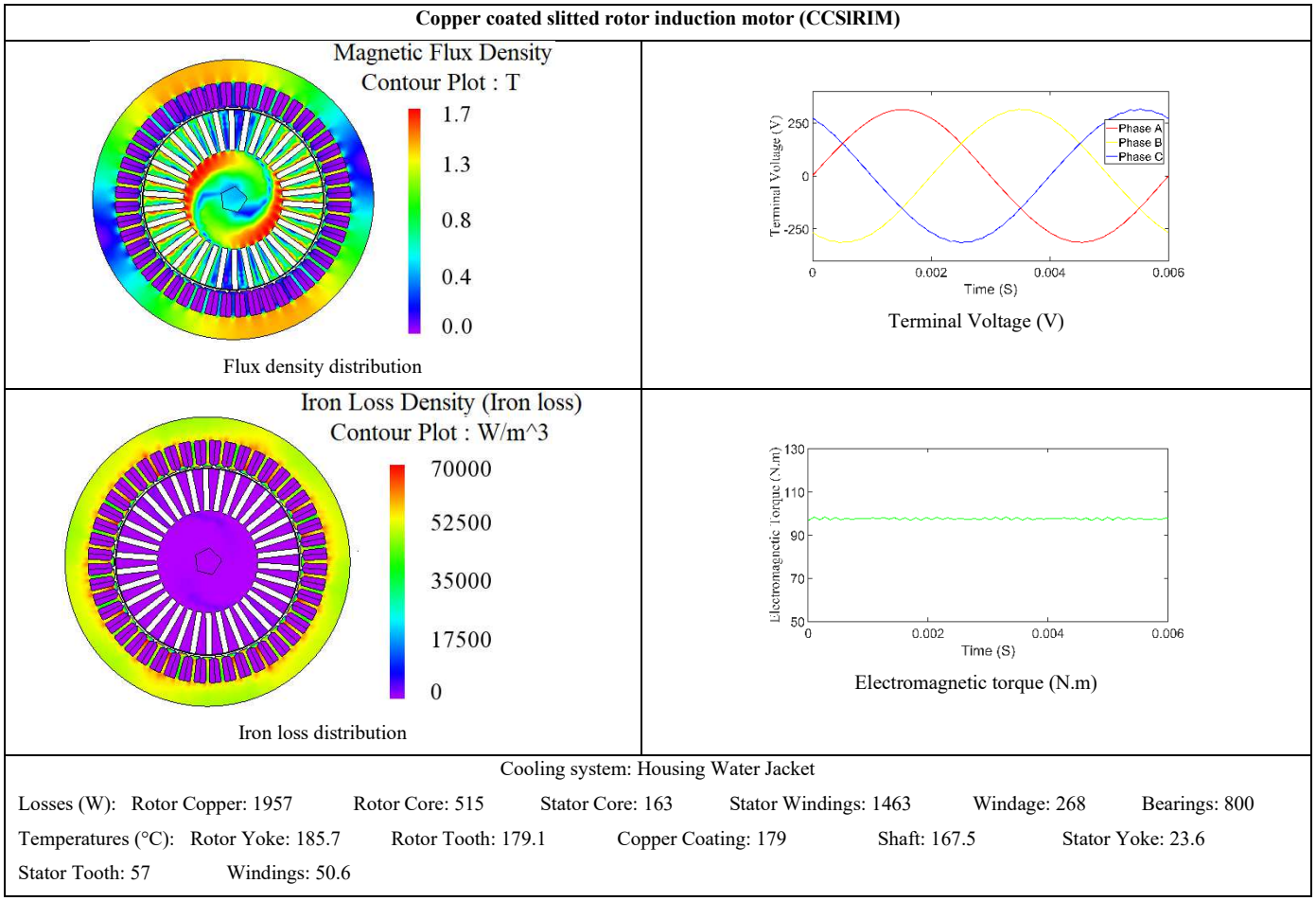


Fig. 11. Magnetic and thermal analysis results of the case study machines

6. TOPSIS/MCDM Analysis and Application-Specific Rankings

In this section, the TOPSIS multi-criteria decision-making method is applied to rank the thirteen machine topologies for two specific FESS applications: frequency regulation in power systems and electric vehicle applications. For this purpose, the evaluation criteria, weighting schemes, ranking results, and sensitivity analysis are presented and discussed. It should be noted that the suitability of FESSs strongly depends on the application duty cycle. Since flywheels may remain at high rotational speeds for extended periods without power transfer, idle and standby losses become a dominant factor in overall system performance [2], [3]. For the electric vehicle application considered in this study, the flywheel is not intended to replace the main energy storage system, which is typically a Li-ion battery, but rather to complement it as a high-power buffer. In this hybrid energy storage concept, the flywheel primarily handles short-duration, high-power events such as acceleration and regenerative braking, while the battery provides the required energy over longer time scales [4]. Although recent advances in Li-ion battery technology have improved energy density and reduced cost, flywheel systems retain clear advantages in terms of power density, rapid response, and extremely high cycle life. Consequently, flywheel energy storage is more appropriately suited to applications characterized by frequent power transients and high cycling, such as grid frequency regulation, power smoothing, and buffering applications, rather than long-duration energy storage in electric vehicles [2], [3].

The optimal selection or prioritization of electrical machine structures for a specific application requires a systematic approach that takes into account a broad set of technical, economic, and operational criteria. Hence, TOPSIS multi-criteria decision-making (MCDM) method may be employed to prioritize and select the most suitable electrical machine type for a specific application. To implement the TOPSIS method, the decision matrix is first constructed. This matrix includes options, selection criteria and weight

of each criterion. In this paper, the thirteen electrical machine types under study serve as the options. In the following sections, the evaluation criteria, determination of weights, and the obtained results for each application scenario are described.

A. Evaluation Criteria

The rows of the decision matrix represent the different options (thirteen electrical machine types), while the columns correspond to the evaluation criteria. The evaluation criteria defined in this paper for comparing the designed electrical machines are:

- C_1: Efficiency
- C_2: Torque density (Nm/kg)
- C_3: Power density (kW/kg)
- C_4: Power factor
- C_5: Torque ripple (%)
- C_6: Robustness (1-10)
- C_7: Cost ($)
- C_8: Mass of cores (kg)
- C_9: Mass of magnet (kg)
- C_{10}: Mass of copper (kg)
- C_{11}: Mass of shaft (kg)
- C_{12}: TRL (Technology Readiness Level) (1-10)
- C_{13}: MRL (Manufacturing Readiness Level) (1-10)
- C_{14}: Lifetime (1-10)
- C_{15}: High temperature design (1-10)
- C_{16}: Manufacturing complexity (1-10)

This comprehensive set of criteria guarantees that both technical performance indicators, such as efficiency, torque density and ripple, and economic and operational indicators, including cost, TRL, MRL and lifetime, are considered. In this study, the efficiency criterion (C_1) is defined as an average efficiency over the operational speed range of the flywheel. Efficiency is evaluated at two representative operating points corresponding to the maximum speed and the minimum speed (assumed to be half of the maximum speed), and the reported efficiency is obtained by averaging the efficiencies at these two speed extremes. This averaged efficiency metric implicitly accounts for idle and standby losses, which dominate flywheel operation during long dwell times at high speed, and therefore provides a realistic and application-relevant measure of electrical machine performance in flywheel energy storage systems.

B. Determination of Criteria Weights

The results of data analysis using the TOPSIS method are influenced by the weights assigned to the criteria. Generally, two approaches are employed for weighting criteria:

- Manual method: In this method, designers determine the weights based on their experience and engineering judgment.
- Automatic method: In this method, the entropy or AHP technique is employed to determine the weights based on the statistical properties of the data.

The particular use of the FESS determines the weights of the evaluation criteria. As a result, two sets of weights were manually determined based on the application context and validated by earlier research in the literature:

- Frequency regulation in power systems: For power system frequency regulation, the electrical machine must deliver fast transient power with frequent charge-discharge cycles. Therefore, for this application, cost and efficiency were considered

the most critical factors, as minimizing operational cost and maximizing energy conversion efficiency are essential for grid services. In contrast, torque density, machine core mass, and power density were assigned relatively lower weights, since the size and power-to-mass ratio are less restrictive in stationary grid applications [2].

- Electric vehicle applications: In traction applications, the highest weightings were given to efficiency, torque density, power density, and cost, which reflects the need for compact, lightweight, and energy-efficient machines [34], [35].

The weighting method ensures that the relative importance of each evaluation criterion is consistent with the practical requirements and constraints of each specific application, providing a logical framework for ranking and selecting the optimal machine topology.

C. TOPSIS Analysis

The performance specifications of the thirteen electrical machine types under study were extracted through FE simulations and analytical evaluations. These data were used to construct the decision matrix, as given in Table 6. The various criteria used in this table have different scales and ranges, and the direct use of raw values may lead to incorrect analysis or misleading results. Therefore, in order to increase the accuracy of comparison and avoid ambiguity, all data are normalized before analysis. With this transformation, all values are placed in a common interval [0,1], allowing them to be compared regardless of the difference in the original unit and scale. To provide a more intuitive visualization of the relative performance of the evaluated machine topologies, a heatmap of the normalized decision matrix is illustrated in Fig. 12. This figure shows the relative contribution of each evaluation criterion to the overall assessment and allows for quick identification of strengths and weaknesses of individual machine topologies. As shown in Fig. 12, the high-ranked machine topologies have high scores in several criteria simultaneously, while lower-ranked candidates tend to have high scores in only a few criteria. Hence, the heatmap provides further insight into the multidimensional nature of the TOPSIS ranking process.

For the frequency regulation case, the weights of each criteria are given in Table 6. By using the TOPSIS method, distances between each machine topology and the positive and negative ideal solutions were determined, and the closeness coefficients were obtained. The final results of this analysis are given in Fig. 13. As shown in this figure, the slitted rotor induction motor (SlRIM) and 4-pole interior permanent magnet motor (4PIPMM) have the highest closeness coefficient (0.802), which makes them the best option for frequency regulation. Their top ranking (0.802) is attributed to their high efficiency, and relatively low cost, which are necessary for use in power systems. The solid rotor induction motor (SoRIM) was ranked second (0.789), with lower efficiency and higher cost. The 2-pole permanent magnet-assisted synchronous reluctance motor (2PPMASRM) was the least preferred candidate because of its high cost and construction complexity.

For electric vehicle applications, a different set of weights has been used to emphasize the most important factors i.e., minimizing volume, and maximizing efficiency, torque and power densities. The weight of criteria for electric vehicle application is given in Table 7. In addition, the TOPSIS analysis results are presented in Fig. 14. The results indicate that the 4-pole surface-mounted permanent magnet motor (4PSMPMM) is the optimal choice for electric vehicle applications, with the highest closeness coefficient (0.842). The 2-pole permanent magnet-assisted synchronous reluctance motor (2PPMASRM) ranked lowest due to its high cost and construction complexity.

Table 6. Weighted decision-making matrix for selecting a high-speed electrical machine for frequency regulation in power systems

		C_1	C_2	C_3	C_4	C_5	C_6	C_7	C_8	C_9	C_{10}	C_{11}	C_{12}	C_{13}	C_{14}	C_{15}	C_{16}
	Type	+	+	+	+	–	+	–	–	–	–	–	+	+	+	+	+
	Weight	20	2	2	7	5	4	20	2	5	3	3	5	4	4	4	10
1	4PPMASRM	95.4	1.2	1.3	0.69	13	6	178.9	46	4.1	16.7	6.5	6	8	8	5	5
2	2PPMASRM	97.6	0.14	0.15	0.61	28.5	6	65.9	52.4	10.2	45.4	6.5	6	8	8	5	5
3	4PSRM	93.8	0.97	0.94	0.55	8.7	7	178.9	46.7	0	16.8	6.5	7	8	9	10	5
4	2PSRM	95.9	0.16	0.16	0.44	47.8	7	65.9	52.4	0	45.4	6.5	7	8	9	10	5
5	4PIPMM	95.1	1.2	1.23	0.94	26.7	6	159.7	37.8	1.8	1.9	4.5	8	8	8	5	6
6	2PIPMM	91.6	0.6	0.58	0.93	23.1	6	503.6	129	5.4	7.7	5	8	8	8	5	6
7	4PSMPMM	96.8	1.5	1.6	0.95	8.5	4	166.9	27.2	1.9	2.6	4.5	8	7	6	5	4
8	2PSMPMM	95.6	0.9	0.96	0.9	2.9	4	361.8	51	3.1	4.4	4.5	8	7	6	5	6
9	SRM	88.2	1.04	1.09	0.18	103	10	265.7	62.5	0	26.9	2.7	8	10	10	10	10
10	CCSlRIM	97	1.1	1.14	0.94	2	9	293.5	55.8	0	30	2.3	8	8	9	10	8
11	CCSoRIM	97	0.93	0.96	0.93	11	10	312.9	70.6	0	31.9	2.3	8	8	9	10	9
12	SlRIM	96	0.71	0.74	0.86	5	9	276.1	105.8	0	27.6	2.3	9	10	9	10	9
13	SoRIM	94	0.65	0.67	0.71	15	10	277.9	119.3	0	27.7	2.3	9	10	10	10	10

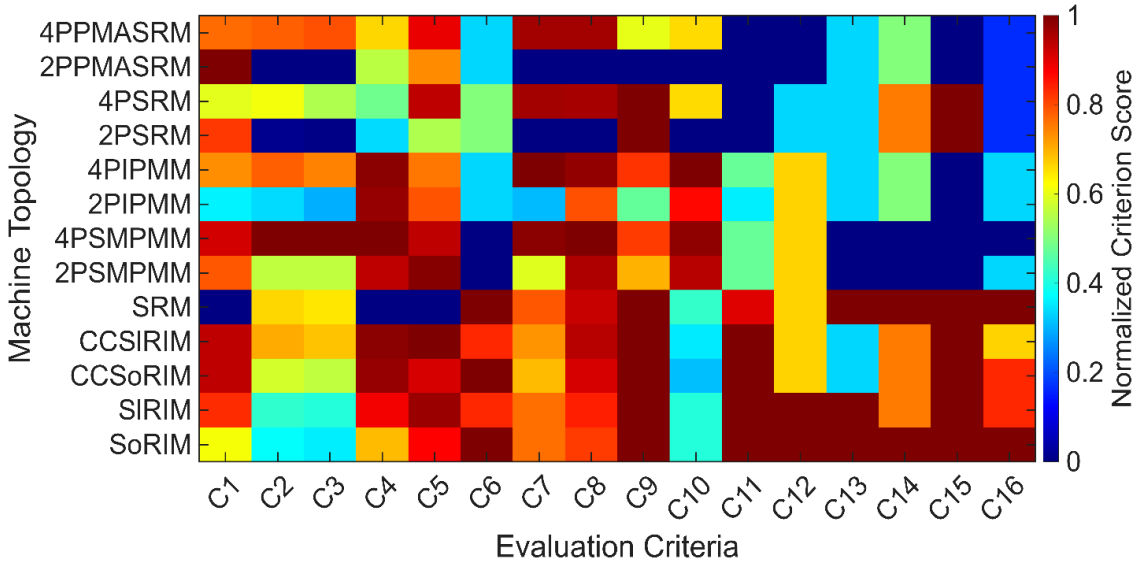


Fig. 12. Normalized performance heatmap of the thirteen machine topologies versus the sixteen evaluation criteria.

Table 7. Weight of criteria for electric vehicle application

	C_1	C_2	C_3	C_4	C_5	C_6	C_7	C_8	C_9	C_{10}	C_{11}	C_{12}	C_{13}	C_{14}	C_{15}	C_{16}
Type	+	+	+	+	–	+	–	–	–	–	–	+	+	+	+	+
Weight	20	15	15	2	6	8	9	3	3	3	1	4	3	4	2	2

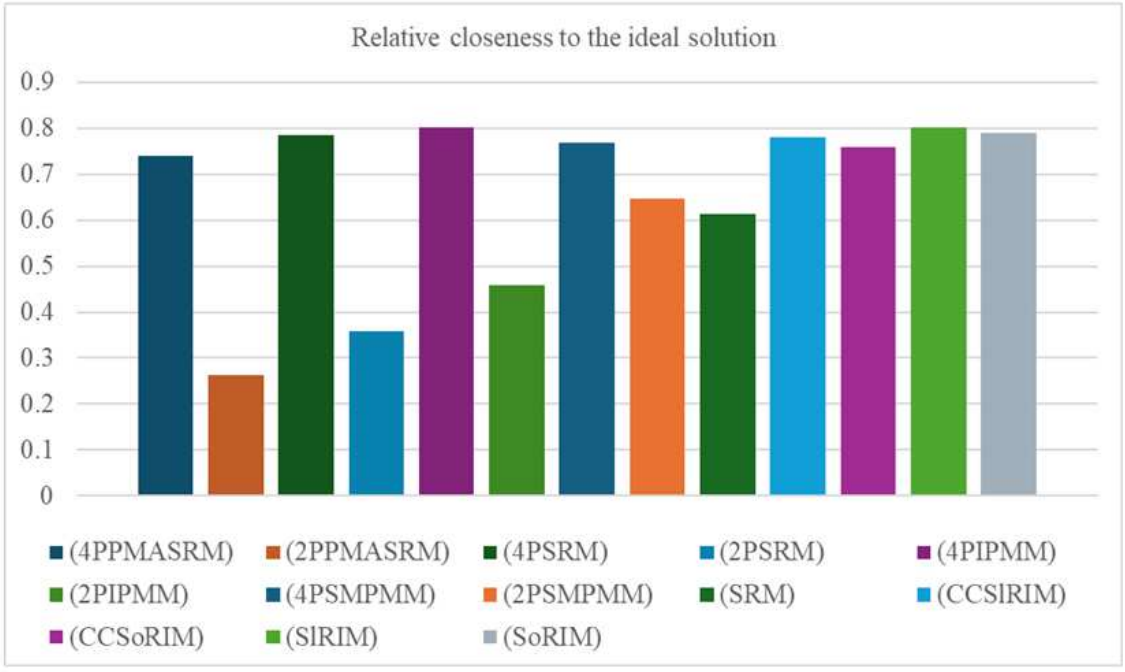


Fig. 13. TOPSIS results for selecting electrical machine topology for use in frequency regulation application

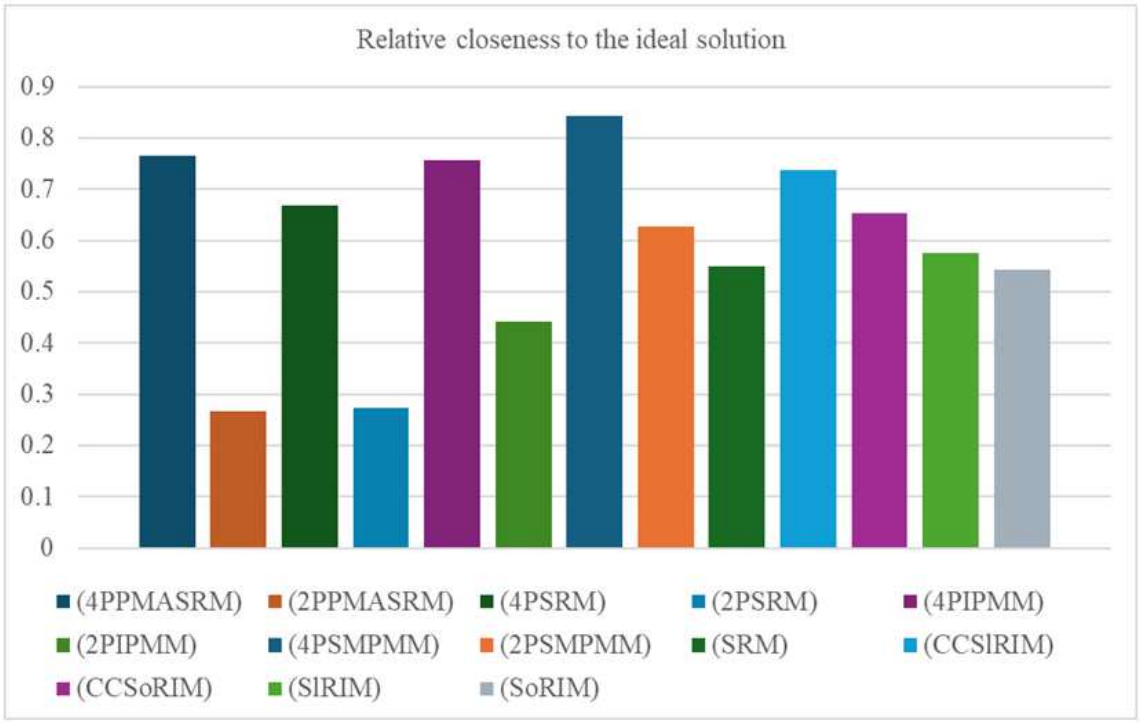


Fig. 14. TOPSIS results for machine topology selection for electric vehicle application

A sensitivity analysis was also performed to test the robustness of the TOPSIS ranking by varying the most influential weighting factors by ±20%. As shown in Table 8, three scenarios were evaluated for the frequency regulation application: the base case (the original weighting scheme), an efficiency-oriented scenario, and a cost-oriented scenario. The results revealed that SlRIM, 4PIPMM, and SoRIM were consistently ranked among the top three machine topologies, with slight changes in relative ordering of the top candidates, and the overall conclusions remained the same. For the electric vehicle application, some other performance-oriented and cost-oriented weighting schemes were also tested. In all scenarios examined, 4PSMPMM maintained the top ranking. These results indicate that moderate variations in weighting factors do not meaningfully affect the overall ranking trends. Therefore, the robustness of the proposed TOPSIS-based decision-making framework is confirmed.

Table 8. Sensitivity analysis of TOPSIS rankings under different weighting scenarios

Application	Scenario	Top-ranked Topologies
Frequency regulation	Base case	SlRIM, 4PIPMM, SoRIM
Frequency regulation	Efficiency-oriented	SlRIM, SoRIM, 4PIPMM
Frequency regulation	Cost-oriented	4PIPMM, SlRIM, SoRIM
Electric vehicle	Base case	4PSMPMM, 4PPMASRM, 4PIPMM
Electric vehicle	Performance-oriented	4PSMPMM, 4PIPMM, 4PPMASRM
Electric vehicle	Cost-oriented	4PSMPMM, 4PPMASRM, CCSlRIM

The suggested framework is purposefully built on established analytical models and design principles documented in the literature. The way these well-known models are methodically incorporated and applied within a single, application-focused design and selection process for FESSs is what makes this work novel. Specifically, a thorough design algorithm is put forth that concurrently takes into account the predominant mechanical, thermal, magnetic, and electrical constraints related to electrical machines functioning in flywheel energy storage systems. Rotor stress, centrifugal forces, and structural integrity at high rotational speeds are examples of mechanical constraints; loss generation, temperature rise, and cooling capability are examples of thermal constraints; magnetic saturation, flux density limits, and demagnetization risk are examples of magnetic constraints; and efficiency, power factor, torque ripple, and loss distribution are examples of electrical constraints. The suggested algorithm incorporates these constraints into a single cohesive design framework, in contrast to traditional methods that usually handle them separately or sequentially. Additionally, a methodology for topology selection and prioritization that is application-oriented is presented. The relative significance of evaluation criteria is modified based on the particular flywheel application, such as electric vehicle applications or power system frequency regulation, each of which places different operational demands on the electrical machine. This makes it possible to compare various machine topologies in an organized and adaptable manner and facilitates well-informed decision-making in the early phases of FESS design. The suggested methodology offers a useful decision-support tool that lowers development risk and cost and directs designers toward appropriate electrical machine structures before experimental prototyping by fusing well-established analytical models with a unified design workflow and an application-dependent decision framework.

7. Discussion, Limitations, and Conclusions

In this study, a comprehensive approach was presented for the optimal selection of high-speed electrical machines used in FESSs, given the key role of the electrical machine in the technical and economic performance of FESSs. For this purpose, an integrated method was proposed, including both the magneto-thermal design of different types of electrical machines and the application of a MCDM technique. Based on this integrated method, thirteen different electrical machine topologies were designed and their electromagnetic and thermal characteristics were extracted to provide a necessary basis for comparison. In addition, using the TOPSIS MCDM method and adjusting the weights of the criteria for two different applications, these thirteen structures were prioritized. The obtained results confirmed that for the frequency control application, the slitted rotor induction motor (SlRIM) and

4-pole interior permanent magnet motor (4PIPMM) were selected as the optimal options, whereas the 2-pole permanent magnet-assisted synchronous reluctance motor (2PPMASRM) ranked lowest. For electric vehicle applications, the 4-pole surface-mounted permanent magnet motor (4PSMPMM) provided the best performance, and the 2-pole permanent magnet-assisted synchronous reluctance motor (2PPMASRM) was considered the least preferred option. This study emphasizes that choosing the optimal structure of the electrical machine depends on the type of application of the FESS, while taking into account the most important criteria for that application. In addition, decision-making and structure selection should not be based solely on general criteria; instead, application-specific requirements, operating conditions, and system constraints should also be considered in the selection process. The findings of this research can provide practical guidance for engineers in the field of optimal design of FESS taking into account mechanical, electromagnetic, and thermal considerations. It should be noted that the rankings and performance metrics obtained here are predictive indicators based on the analytical and FE models employed, and not guaranteed performance values across all practical operating conditions. The performance of a particular machine topology may be affected by manufacturing tolerances, material variations, control strategies, operating environments, and system-level integration constraints that were not considered in the present study.

Limitations and Future Work: While the multiphysics design framework presented in this study is comprehensive, there are still some limitations that should be recognized. First, the findings are derived from analytical calculations and FEA simulations. At this stage, physical testing of all thirteen designed topologies was not feasible due to the high manufacturing costs and safety concerns. The main objective of this study is to conduct a comprehensive and fair comparative evaluation of the different machine structures using the developed algorithms before undertaking costly prototyping. In future work, two to three of the highest-ranked topologies identified using the proposed method will be fabricated and experimentally validated. These experimental results will be used to compare with the simulation outcomes and verify the accuracy of the proposed algorithms, and the corresponding results will be reported in future publications. Second, the critical speed calculations are derived from simplified analytical models and do not incorporate the full coupled dynamics of the flywheel, rotor, and magnetic bearings. Third, the windage loss model used in this study does not account for molecular-flow effects at extremely low vacuum pressures, and more advanced models of vacuum loss should be considered. Fourth, the operating behavior of FESS applications was modeled using simplified operating assumptions rather than detailed real-world duty cycles and lifetime loading profiles. Fifth, in this study, weighting factors used in the TOPSIS analysis were assigned based on engineering judgment and literature; therefore, other weighting methods such as entropy, AHP, or CRITIC may lead to different ranking outcomes. Finally, all machine topologies were designed using steel-based rotors. Future works may extend the proposed framework to hybrid rotor configurations, incorporate advanced rotordynamic models, perform experimental validation, and consider long-term operational and economic performance under realistic operating conditions.

CRediT authorship contribution statement

H. AM.: Conceptualization, Formal analysis, Investigation, Methodology, Validation, Writing – original draft.

R. M.: Conceptualization, Data curation, Formal analysis, Investigation, Methodology, Validation, Writing – original draft, Writing – review & editing.

Declaration of competing interest

The authors declare that they have no known competing financial interests or personal relationships that could have appeared to influence the work reported in this paper.

Data availability

Data including the geometric dimensions, thermal model parameters, and cooling-system configurations of all investigated machines are provided in the Supplementary Material associated with this article.

Funding

Not applicable.

References

[1] W. Ji *et al.*, "Applications of flywheel energy storage system on load frequency regulation combined with various power generations: A review," *Renew. Energy*, vol. 223, p. 119975, 2024, doi: https://doi.org/10.1016/j.renene.2024.119975.

[2] M. E. Amiryar and K. R. Pullen, "A review of flywheel energy storage system technologies and their applications," *Appl. Sci.*, vol. 7, no. 3, p. 286, 2017.

[3] X. Li and A. Palazzolo, "A review of flywheel energy storage systems: state of the art and opportunities," *J. Energy Storage*, vol. 46, p. 103576, 2022.

[4] S. F. Tie and C. W. Tan, "A review of energy sources and energy management system in electric vehicles," *Renew. Sustain. energy Rev.*, vol. 20, pp. 82–102, 2013.

[5] N. M. Ingale and V. M. Mankar, "Design of energy storage system with flywheel and electrical drives," *Int. Conf. Signal Process. Commun. Power Embed. Syst. SCOPES 2016 - Proc.*, pp. 2074–2077, 2017, doi: 10.1109/SCOPES.2016.7955813.

[6] S. Choudhury, "Flywheel energy storage systems: A critical review on technologies, applications, and future prospects," *Int. Trans. Electr. Energy Syst.*, vol. 31, no. 9, pp. 1–26, 2021, doi: 10.1002/2050-7038.13024.

[7] C. Bianchini, A. Torreggiani, D. David, and A. Bellini, "Design of Motor/Generator for Flywheel Batteries," *IEEE Trans. Ind. Electron.*, vol. 68, no. 10, pp. 9675–9684, 2021, doi: 10.1109/TIE.2020.3026292.

[8] A. G. Olabi, T. Wilberforce, M. A. Abdelkareem, and M. Ramadan, "Critical review of flywheel energy storage system," *Energies*, vol. 14, no. 8, pp. 1–33, 2021, doi: 10.3390/en14082159.

[9] R. Takarli *et al.*, "A Comprehensive Review on Flywheel Energy Storage Systems: Survey on Electrical Machines, Power Electronics Converters, and Control Systems," *IEEE Access*, vol. 11, no. August, pp. 81224–81255, 2023, doi: 10.1109/ACCESS.2023.3301148.

[10] Y. Yu, Y. Wang, and F. Sun, "The latest development of the motor/generator for the flywheel energy storage system," *Proc. 2011 Int. Conf. Mechatron. Sci. Electr. Eng. Comput. MEC 2011*, pp. 1228–1232, 2011, doi: 10.1109/MEC.2011.6025689.

[11] X. Lian, C. Caruana, M. Galea, and R. Camilleri, "Design of a high specific power permanent magnet electrical machine for a flywheel energy storage system," in *2023 26th International Conference on Electrical Machines and Systems (ICEMS)*, IEEE, 2023, pp. 2381–2386. doi: 10.1109/ICEMS59686.2023.10344436.

[12] W. Gruber, T. Hinterdorfer, H. Sima, A. Schulz, and J. Wassermann, "Comparison of different motor-generator sets for long term storage flywheels," *2014 Int. Symp. Power Electron. Electr. Drives, Autom. Motion, SPEEDAM 2014*, pp. 161–166, 2014, doi: 10.1109/SPEEDAM.2014.6871987.

[13] M. G. Kesgin, P. Han, N. Taran, and D. M. Ionel, "Overview of flywheel systems for renewable energy storage with a design study for high-speed axial-flux permanent-magnet machines," *8th Int. Conf. Renew. Energy Res. Appl. ICRERA 2019*, pp. 1026–1031, 2019, doi: 10.1109/ICRERA47325.2019.8996526.

[14] L. Zhou and Z. Qi, "Review of flywheel energy storage system," *ISES Sol. World Congr. 2007, ISES 2007*, vol. 4, no. May, pp. 2815–2819, 2007, doi: 10.1007/978-3-540-75997-3_568.

[15] A. Soomro, M. E. Amiryar, D. Nankoo, and K. R. Pullen, "Performance and loss analysis of squirrel cage induction machine based flywheel energy storage system," *Appl. Sci.*, vol. 9, no. 21, 2019, doi: 10.3390/app9214537.

[16] J. De Santiago and J. G. de Oliveira, *Electric Machine Topologies in Energy Storage Systems*. Energy Storage. IntechOpen, 2010.

[17] X. Dai, X. Ma, D. Hu, J. Duan, and H. Chen, "An Overview of the R&D of Flywheel Energy Storage Technologies in China," *Energies*, vol. 17, no. 22, 2024, doi: 10.3390/en17225531.

[18] R. Sebastián and R. P. Alzola, “Flywheel energy storage systems: Review and simulation for an isolated wind power system,” *Renew. Sustain. Energy Rev.*, vol. 16, no. 9, pp. 6803–6813, 2012.

[19] M. E. Amiryar and K. R. Pullen, “Analysis of standby losses and charging cycles in flywheel energy storage systems,” *Energies*, vol. 13, no. 17, p. 4441, 2020.

[20] B. H. Kenny, P. E. Kascak, R. Jansen, T. Dever, and W. Santiago, “Control of a high-speed flywheel system for energy storage in space applications,” *IEEE Trans. Ind. Appl.*, vol. 41, no. 4, pp. 1029–1038, 2005.

[21] X. Li, D. Dietz, J. An, N. Erd, Y. Gemeinder, and A. Binder, “Manufacture and testing of a magnetically suspended 0.5-kWh flywheel energy storage system,” *IEEE Trans. Ind. Appl.*, vol. 58, no. 5, pp. 6152–6162, 2022.

[22] D. Bender, “Flywheels,” in *Energy Storage Handbook*, Sandia National Laboratories, 2022. [Online]. Available: https://www.sandia.gov/app/uploads/sites/163/2022/03/ESHB_Ch07_Flywheels_Bender.pdf

[23] G. Reichert and G. Pasquarella, “High speed electric machines, status, trends and problems,” 1995.

[24] S. P. Timoshenko and J. N. Goodier, *Theory of Elasticity*, 3rd ed. McGraw-Hill, New York, 1970. [Online]. Available: https://digital.admtec.org.br/fetch.php/primo explore/IsmBNv/Timoshenko_Goodier_Theory_Of_Elasticity.pdf

[25] F. Viggiano and G. Schweitzer, “Active magnetic support and design of high speed rotors for powerful electric drives,” in *Proceedings of the Third International Symposium on Magnetic Bearings*, 1992, pp. 549–558.

[26] F. G. Zhang, G. Du, T. Y. Wang, and G. Liu, “Review on development and design of high speed machines,” *Trans. China Electrotech. Soc.*, vol. 31, no. 7, pp. 1–18, 2016.

[27] R. Lateb, J. Enon, and L. Durantay, “High speed, high power electrical induction motor technologies for integrated compressors,” *Proc. - 12th Int. Conf. Electr. Mach. Syst. ICEMS 2009*, 2009, doi: 10.1109/ICEMS.2009.5382960.

[28] J. Huppunen, *High-speed solid-rotor induction machine–electromagnetic calculation and design*. Lappeenranta University of Technology, 2004.

[29] T. Aho, “Electromagnetic Design of a Solid Steel Rotor Motor for Demanding Operation Environments,” Acta Universitatis Lappeenrantaensis, 2007.

[30] J. Lähteenmäki, “Design and Voltage Supply of High-Speed Induction Machines,” Helsinki University of Technology, 2002.

[31] O. Aglen and A. Andersson, “Thermal analysis of a high-speed generator,” in *38th IAS Annual Meeting on Conference Record of the Industry Applications Conference, 2003.*, IEEE, 2003, pp. 547–554.

[32] Y.-K. Kim, M.-C. Choi, K.-H. Suh, Y.-C. Ji, and D.-S. Wang, “High-speed induction motor development for small centrifugal compressor,” in *ICEMS’2001. Proceedings of the Fifth International Conference on Electrical Machines and Systems (IEEE Cat. No. 01EX501)*, IEEE, 2001, pp. 891–894.

[33] J. Pyrhönen, J. Nerg, P. Kurronen, and U. Lauber, “High-speed high-output solid-rotor induction-motor technology for gas compression,” *IEEE Trans. Ind. Electron.*, vol. 57, no. 1, pp. 272–280, 2010, doi: 10.1109/TIE.2009.2021595.

[34] Q. Shen *et al.*, “Design and Analysis of the High-Speed Permanent Magnet Motors: A Review on the State of the Art,” *Machines*, vol. 10, no. 7, 2022, doi: 10.3390/machines10070549.

[35] T. Gammaidoni, J. Zembi, M. Battistoni, G. Biscontini, and A. Mariani, “CFD analysis of an electric motor’s cooling system: Model validation and solutions for optimization,” *Case Stud. Therm. Eng.*, vol. 49, p. 103349, 2023.

[36] W. Le, M. Lin, K. Lin, L. Jia, and S. Wang, “A rotor cooling enhanced method for axial flux permanent magnet synchronous machine with housing-cooling,” *IEEE Trans. Appl. Supercond.*, vol. 31, no. 8, pp. 1–5, 2021.

[37] P. König, D. Sharma, K. R. Konda, T. Xie, and K. Höschler, “Comprehensive review on cooling of permanent magnet synchronous motors and their qualitative assessment for aerospace applications,” *Energies*, vol. 16, no. 22, p. 7524, 2023.

[38] D. Staton, A. Boglietti, and A. Cavagnino, “Solving the more difficult aspects of electric motor thermal analysis,” in *IEEE International Electric Machines and Drives Conference, 2003. IEMDC’03.*, IEEE, 2003, pp. 747–755.

[39] A. Tüysüz, F. Meyer, M. Steichen, C. Zwyssig, and J. W. Kolar, “Advanced cooling methods for high-speed electrical machines,” *IEEE Trans. Ind. Appl.*, vol. 53, no. 3, pp. 2077–2087, 2017.

[40] C. T. Krasopoulos, A. S. Ioannidis, A. F. Kremmydas, I. A. Karafyllakis, and A. G. Kladas, “Convection heat transfer coefficient

regression models construction for fast high-speed motor thermal analysis," *IEEE Trans. Magn.*, vol. 58, no. 11, pp. 1–5, 2022.

[41] S. Wu, D. Hao, and W. Tong, "Cooling system design and thermal analysis of modular stator hybrid excitation synchronous motor," *CES Trans. Electr. Mach. Syst.*, vol. 6, no. 3, pp. 241–251, 2022.

[42] M. Sun, Y. Xu, and W. Zhang, "Multiphysics analysis of flywheel energy storage system based on cup winding permanent magnet synchronous machine," *IEEE Trans. Energy Convers.*, vol. 38, no. 4, pp. 2684–2694, 2023.

[43] F. P. McCluskey, Y. Saadon, Z. Yao, and A. Camacho, "Cooling for electric aircraft motors," in *2019 18th IEEE Intersociety Conference on Thermal and Thermomechanical Phenomena in Electronic Systems (ITherm)*, IEEE, 2019, pp. 1134–1138.

[44] S. K. Thangaraju, K. M. Munisamy, and S. Rajoo, "Numerical investigation on cooling performance of oil cooled PMSM jacket design with vertical straight fin design," *Int. J. Thermofluids*, vol. 16, p. 100209, 2022.

[45] G. Venturini, G. Volpe, and M. Popescu, "Slot water jacket cooling system for traction electrical machines with hairpin windings: Analysis and comparison," in *2021 IEEE International Electric Machines & Drives Conference (IEMDC)*, IEEE, 2021, pp. 1–6.

[46] S. Wu, D. Hao, and W. Tong, "Temperature field analysis of mine flameproof outer rotor permanent magnet synchronous motor with different cooling schemes," *CES Trans. Electr. Mach. Syst.*, vol. 6, no. 2, pp. 162–169, 2022.

[47] M. R. Guechi, P. Desevaux, P. Baucour, C. Espanet, R. Brunel, and M. Poirot, "Spray cooling of electric motor coil windings," *J. Comput. Multiph. Flows*, vol. 8, no. 2, pp. 95–100, 2016.

[48] P. S. Ghahfarokhi, A. Podgornovs, A. Kallaste, T. Vaimann, A. Belahcen, and A. J. M. Cardoso, "Oil spray cooling with hairpin windings in high-performance electric vehicle motors," in *2021 28th International Workshop on Electric Drives: Improving Reliability of Electric Drives (IWED)*, IEEE, 2021, pp. 1–5.

[49] Z. Zhang, Q. Song, and B. Ahmed, "Optimized flow rate and efficient shaft water cooling method for EV's PMSM temperature-dependent energy system output power increase," *Case Stud. Therm. Eng.*, vol. 61, p. 104901, 2024.

[50] H. Wang, X. Liu, M. Kang, L. Guo, and X. Li, "Oil injection cooling design for the IPMSM applied in electric vehicles," *IEEE Trans. Transp. Electrif.*, vol. 8, no. 3, pp. 3427–3440, 2022.

[51] W. Pan, J. Ma, X. Dong, J. Guo, and F. Wang, "Numerical study of jet impingement cooling methods for improving heat transfer in a flywheel energy storage system," *J. Energy Storage*, vol. 95, p. 112408, 2024.